FATIGUE CRACK GROWTH ANALYSIS MODELS FOR FUNCTIONALLY GRADED MATERIALS

A THESIS SUBMITTED TO
THE GRADUATE SCHOOL OF NATURAL AND APPLIED SCIENCES
OF
MIDDLE EAST TECHNICAL UNIVERSITY

BY

BARIŞ SABUNCUOĞLU

IN PARTIAL FULLFILLMENT OF THE REQUIREMENTS
FOR
THE DEGREE OF MASTER OF SCIENCE
IN
MECHANICAL ENGINEERING

JANUARY 2006

Approval of the Graduate School of Natural and Applied Sciences

Prof. Dr. Canan ÖZGEN
Director

I certify that this thesis satisfies all the requirements as a thesis for the degree of Master of Science.

Prof. Dr. Kemal İDER
Head of Department

This is to certify that we have read this thesis and that in our opinion it is fully adequate, in scope and quality, as a thesis for the degree of Master of Science.

Asst. Prof. Dr. Serkan DAĞ
Supervisor

Examining Committee Members

Prof. Dr. Metin AKKÖK	(METU-ME)	
Asst. Prof. Dr. Serkan DAĞ	(METU-ME)	
Prof. Dr. Levend PARNAS	(METU-ME)	
Asst. Prof. Dr. Merve ERDAL	(METU-ME)	
Dr. Özge ŞEN	(TÜBİTAK-SAGE)	

I hereby declare that all information in this document has been obtained and presented in accordance with academic rules and ethical conduct. I also declare that, as required by these rules and conduct, I have fully cited and referenced all material and results that are not original to this work.

Name, Last name: BARIŞ SABUNCUOĞLU

Signature:

ABSTRACT

FATIGUE CRACK GROWTH ANALYSIS MODELS FOR FUNCTIONALLY GRADED MATERIALS

Sabuncuoğlu, Barış

M.S., Department of Mechanical Engineering

Supervisor: Asst. Prof. Dr. Serkan Dağ

January 2006, 92 pages

The objective of this study is to develop crack growth analysis methods for functionally graded materials under mode I cyclic loading by using finite element technique. The study starts with the analysis of test specimens which are given in ASTM standard E399. The material properties of specimens are assumed to be changing along the thickness direction according to a presumed variation function used for the modeling of functionally graded materials. The results of the study reveal the influence of different material variation functions on the crack growth behavior.

In the second part, the growth of an elliptical crack which is a common case in engineering applications is analyzed. First, mode I cycling loading is applied perpendicular to the crack plane and crack growth profiles for a certain number of cycles are obtained for homogeneous materials. Then, the code is extended for the analysis functionally graded materials. The material properties are assumed to vary as an exponential function along the major or minor axis direction of the crack. The results can be used to examine the crack profile and material constants' influence for a certain number of cyclic loading.

Keywords: Functionally Graded Materials, Fatigue Crack Growth, Finite Element Method, Elliptical Crack

ÖZ

FONKSİYONEL OLARAK DERECELENDİRİLMİŞ MALZEMELER İÇİN YORULMA ÇATLAĞI İLERLEMESİ ANALİZ MODELLERİ

Sabuncuoğlu, Barış
Yüksek Lisans, Makina Mühendisliği Bölümü
Tez Yöneticisi: Y.Doç.Dr. Serkan Dağ

Ocak 2006, 92 sayfa

Bu çalışmanın başlıca amacı, mod I çevrimsel yük altındaki foksiyonel derecelendirilmiş malzemelerde sonlu eleman yöntemi kullanılarak yorulma çatlağı ilerlemesi analiz yöntemi geliştirilmesidir. Çalışmaya ASTM E399 standardında verilen test numunelerinin analizleri ile başlanmıştır. Fonksiyonel derecelendirilmiş malzemenin modellenmesi için malzeme özelliklerinin kalınlık boyunca değişim fonksiyonuna göre değiştiği varsayılmıştır. Sonuçlar farklı değişim fonksiyonlarının çatlak ilerleme davranışına etkisini göstermektedir.

İkinci bölümde, mühendislik uygulamalarında sıkça rastlanan eliptik çatlağın ilerlemesi incelenmiştir. Öncelikle, homojen malzeme için çatlak düzlemine dik mod I çevrimsel yük uygulanarak, belirli çevrim sayısı kadar çatlak ilerleme profilleri elde edilmiştir. Daha sonra kod, fonksiyonel derecelendirilmiş malzemeler için geliştirilmiştir. Malzeme özelliklerinin çatlağın majör veya minör eksenleri boyunca üstel fonksiyonla değiştiği varsayılmıştır. Sonuçlar, çatlak profilinin ve malzeme özelliklerinin etkisinin incelenmesine olanak sağlamıştır.

Anahtar Kelimeler: Fonksiyonel Olarak Derecelendirilmiş Malzeme, Yorulma Çatlağı İlerlemesi, Sonlu Elemanlar Yöntemi, Eliptik Çatlak

To My Family

ACKNOWLEDGEMENTS

I would like to express my gratitutes to my supervisor Asst. Prof. Dr. Serkan Dağ for his help and guidance throughout the course of this study. His positive outlook and confidence in my research inspired me and encouraged me for the successive of this thesis.

I would also like to thank my parents Saadet and Tezer Sabuncuoğlu and my sister Dr. Deniz Sabuncuoğlu Tezcan throughout this study for all their love, patience and encouragement.

It would be very difficult for me to study efficiently without the help of my colleagues at TÜBİTAK-SAGE; Özlem Sökmen, in creating the APDL codes and Suat Ege Yıldızoğlu, for sharing his knowledge about MATLAB. I cannot forget to mention my boss Dr. Serkan Gözübüyük for his support.

Also I would like to thank to my friends Sümeyra Sayman, Emre Selvi and Yetiş Uysal for their advices during the work.

And lastly, very special thanks to my friend Suna Atasayar for never leaving me alone during the study.

Finite element analyses which are carried out on ANSYS were performed using the facilities at TÜBİTAK-SAGE, which is greatly acknowledged.

TABLE OF CONTENTS

LIST OF TABLES

LIST OF FIGURES

LIST OF SYMBOLS

$f\left(\frac{a}{W}\right)$	Non-dimensional stress intensity factor
a	Crack length in 2D analyses, crack length in minor axis direction in elliptical crack
b	Binormial direction at a point on crack front
B	Specimen thickness
c	Crack length in major axis direction in elliptical crack
C	Paris – Erdoğan Law constant
CR	Ceramic rich
E	Modulus of elasticity
FGM	Functionally graded material
H	Width in surface crack problem
HC	Homogeneous ceramic
K_C, K_{IC}, K_{IIC}, K_{IIIC}	Plane stress, mode I, II, III critical stress intensity factors
K_I, K_{II}, K_{III}	Mode I, II, III stress intensity factors
K_{th}	Threshold stress intensity factor
LN	Linear variation
m	Normal direction at a point on crack front
MR	Metal rich
N	Number of cycles
n	Paris – Erdoğan Law exponent
n	Paris – Erdoğan Law exponent
$\emptyset$	Parametric angle along the elliptical crack
P	Applied cyclic load
R	Distance along crack opening direction
r	Radial distance in polar coordinate system
r_1	Inner radius of arc bend specimen

r_2	Outer radius of arc bend specimen
s	Arc length of crack front
S	Span distance in bend bar specimen
SIF	Stress intensity factor
t	Tangential direction on crack front
u_x	Displacement in x direction
W	Specimen width
β	Constant in material variation function
θ	Angle in polar coordinate system
ν	Poisson's ratio
σ_{xx}	Stress in x direction

CHAPTER 1

INTRODUCTION TO FUNCTIONALY GRADED MATERIALS

1.1 The Concept of Functionally Graded Materials

With the rapid development of aircraft and space vehicles, the materials to withstand severe environments such as very high temperatures and large temperature gradients in diesel and turbine engines are demanded [1]. In general the materials science engineers tend to go after homogeneous structures. The main attraction was towards the ceramic structures which are very resistant to oxidation and creep at very high temperatures. Also they are usually stiff structures and resistant to high mechanical loading. Nevertheless their toughness being very low becomes always a great problem in severe conditions. There are many new ceramic materials developed for this problem but their material properties never exhibit the advantages of metallic materials properties in structures. Metals are very appropriate when toughness, high strength and fracture resistance are of concern but at high temperature applications ceramics are more resistant to loss of structural integrity (Table 1.1). Direct application of ceramic coating also causes poor bonding with metals and under cyclic thermal or mechanical loads they tend to release from metal surface.

Table 1.1 Comparison of metals and ceramics

	Strength	***Toughness***	***Fracture resistance***	***Oxidation***	***Heat Insulation***
Metals	Good	Good	Good	Poor	Poor
Ceramics	Poor	Poor	Poor	Good	Good

The idea of functionally graded materials was first proposed by Niino and Maeda [2]. The aim of this study was the development of super heat-resistant materials for the space research. It was mentioned that fracturing induced by large thermal stresses due to the mismatch of thermal expansion is a very significant problem. As advanced materials to resolve the problem, Functionally Gradient Material (FGM) has been proposed in this study.

FGMs are two-phase particulate composites produced in such a way that the volume fractions of the constituents vary continuously in the thickness direction to give a predetermined composition profile. This profile variation ceramic to metal near the surface is produced in such a way that the resulting non-homogeneous material has the desired thermomechanical properties.

Figure 1.1 shows the microstructure of an FGM with 5 layers of coating starting from NiCoCrAlY to YSZ that are used as thermal barrier coatings. As it is seen, a gradual increase in ceramic content ends the structure with 100% ceramic material.

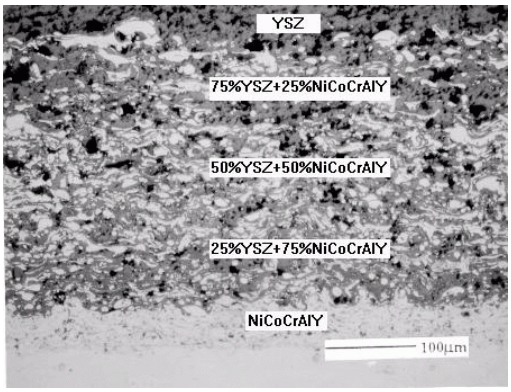

Figure 1.1. Microstructure of functionally graded YSZ/NiCoCrAlY coating [1]

1.2 Application Areas of FGM Materials

The main application area of these materials is aerospace engineering. Typical applications include thermal barrier coatings for engines and airframes of space planes [1,3]. However, they are also used in different areas such as sensor and energy applications. One example is the implementation of dielectric thin-film stacks for capacitors (Figure 1.2) [4]. Another application area of FGMs are artifical implants in biomedical studies. Figure 1.3 represents a functionally graded implant for cranial reconstruction in case of a head surgery [5].

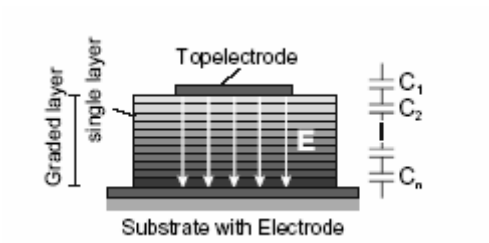

Figure 1.2. Schematic cross section of a graded dielectric thin film [4]

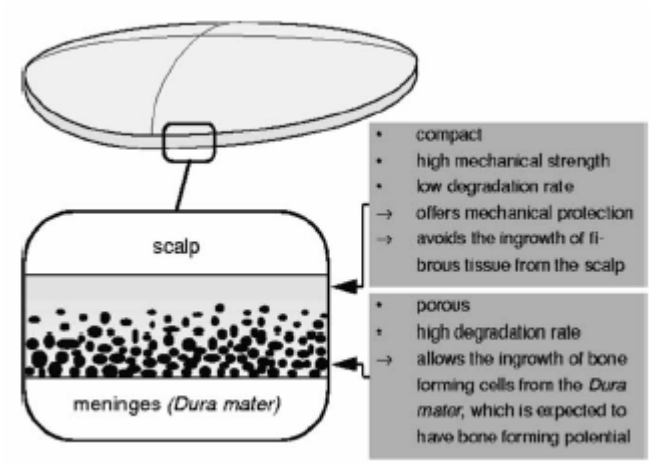

Figure 1.3. Concept of a functionally graded implant for cranial reconstruction [5]

1.3 Processing of FGM Materials

The manufacturing process of an FGM can usually be divided in building the spatially inhomogeneous structure (gradation) and transformation of this structure into a bulk material (consolidation). Gradation processes can be classified as constitutive, homogenizing and segregating processes. Advances in automation technology during the last decades have rendered gradation processes technologically and economically viable [6,7].

There are many processing techniques of FGMs but most frequently used ones are, Plasma Spraying, Electron Beam Physical Vapor Deposition (EB-PVD).

1.3.1 Plasma Spraying

In plasma spraying, a deposited layer is formed through the sequential build-up of splats. Three processing methods exist for plasma spray processing of FGMs. These three methods can be classified as follows:

- Single torch systems-utilizing multiple feeders and blended or composite powders.
- Multiple torch systems-employing independent feeding systems for each component (Figure 1.4).
- Process combinations-using wire/powder feed system combinations.

Each technique has its own advantages and limitations. Process combinations offer different approaches for creating unique microstructures [8].

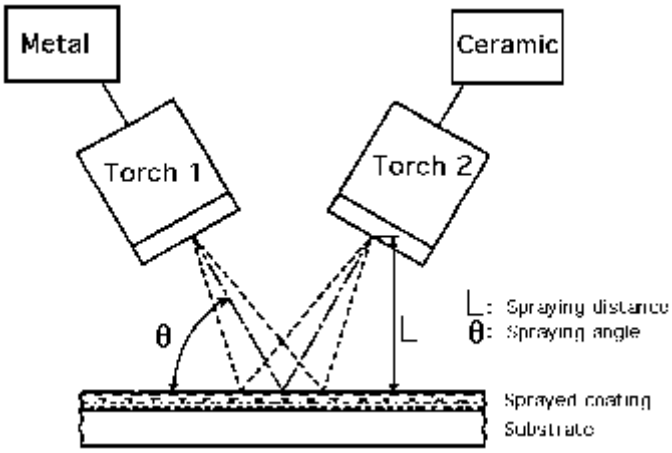

Figure 1.4. Plasma spraying technique multiple torch systems [8]

1.3.2 Electron Beam Physical Vapor Deposition (EB-PVD)

The principle of this technique is the electron beam evaporation from one source of mixtures of metals and ceramics with different vapour pressures at the evaporation temperature. By this method, replacing the flat metal–ceramic interface by a gradient transition zone and achieving a good adhesion of the coating to the substrate are possible. Several variants of EB-PVD technique are utilized [9,10]. Evaporation by the electron beam of a metal ceramic tablet placed into a copper water-cooled crucible, is the simplest technological variant. The structure is given in Figure 1.5. In this method, a tablet of a mixture of metallic powders and ceramics is produced by compacting and subsequent annealing in vacuum. Tablet evaporation is, as a rule, performed with the electron beam of a variable power. Tablet heating is initially performed with a low-power beam. Then, the beam current is gradually increased by a certain program and the tablet is evaporated completely [9].

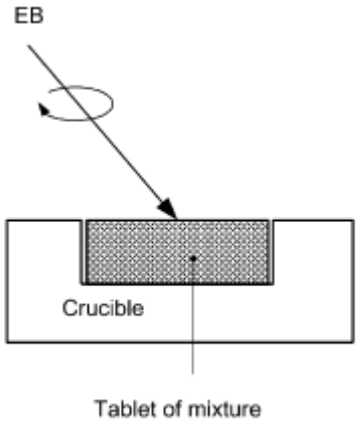

Figure 1.5. Tablet evaporation [9].

1.4 Definition of Material Properties in FGM Studies

When dealing with fracture mechanics problems, evaluation of material properties are very important. Because of the nonhomogenity in the structure, the material properties are not constant throughout the FGM structure. Among the previous studies Erdoğan and Wu [11] considered the surface and subsurface cracks. Öztürk and Erdoğan [12] and Fildis and Yahşi [13] studied on the axisymmetric crack problem in a nonhomogeneous medium. Dağ [14] made a study to determine the thermal stress intensity factors in a thin walled FGM cylinder which contains a circumferential crack. Yıldırım *et al.* [15] analyzed three dimensional crack problems in FGM coatings. Tilbrook *et al.* [16] investigated crack propagation and fracture of alumina/epoxy composite FGMs.

In all of these studies, the variations of material properties are assumed to be in thickness direction with different volumetric ratios of ceramic and metallic materials. In order to be consistent with these studies, the mechanical properties are assumed to be varying in thickness direction according to volumetric ratios of materials.

As can be seen in Figure 1.6, material properties vary along the thickness from 100% metal to 100% ceramic depending on the metal and ceramic percentages. By fitting a curve through these points, variation of material properties can be defined.

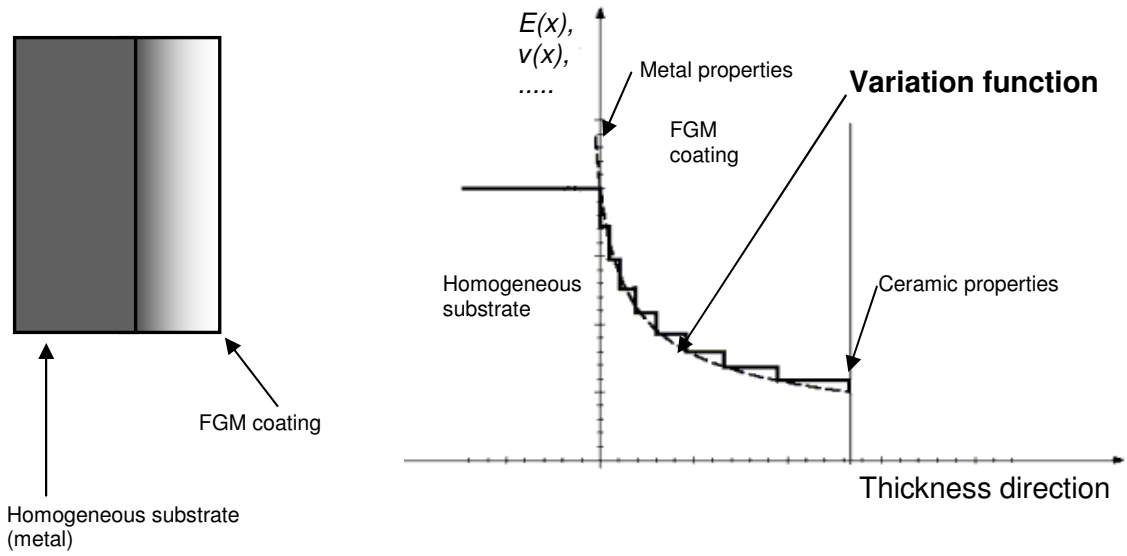

Figure 1.6. The definition of material properties

CHAPTER 2

FRACTURE MECHANICS OF FUNCTIONALLY GRADED MATERIALS

As it is discussed before, functionally graded materials open new possibilities for optimizing both material and component structures to achieve high performance and material efficiency. However, at the same time, it also brings challenging mechanics problems including the understanding of damage and fracture behavior of such materials because of the generation of orthotropy and nonhomogeneity due to the material processing technique utilized. [17]

Fracture behavior of nonhomogeneoeus materials is widely studied till now. Gu and Asaro [18] performed theoretical studies in a four point bending specimen consisting of orthotropic FGMs. Ozturk and Erdogan [19,20] used integral equations to investigate mode I and mixed-mode crack problems in an infinite non-homogeneous orthotropic medium with a crack aligned with one of the principal directions.

In this study, the evaluation of stress intensity factors at the crack tip will be achieved via the finite element method in conjunction with the displacement correlation technique.

2.1 Displacement Correlation Technique

This is a widely used technique in evaluating the stress intensity factors via FEM. Kim and Paulino [17] evaluated mode I and mixed-mode two-dimensional problems and compared them to the analytical results of Ozturk and Erdogan [20].

Wawrzynek *et al.* [21] worked on modeling of fatigue crack growth in spiral bevel gears. Phan *et al.* [22] studied the numerical modeling of crack stability and propagation for the accurate determination of stress intensity factors (SIFs).

In this study, displacement correlation technique is utilized by the application of linear elastic fracture mechanics. A three-dimensional crack front under mode I loading as shown in Figure 2.1 is considered [15].

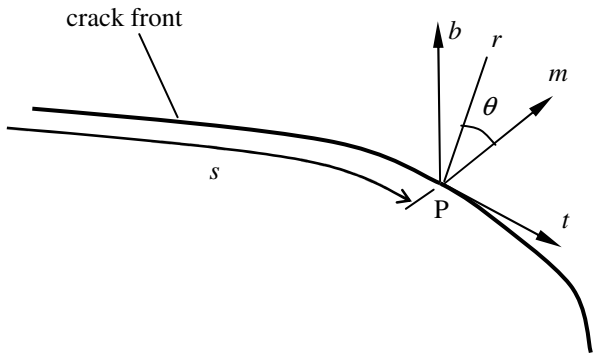

Figure 2.1. Crack front and the local coordinate system [15]

The crack front is assumed to be embedded in an FGM. The parameter s in Figure 2.1 is the arc length of the crack front and t, m, b are the axes of the local coordinate system located at point P composed of the tangential (t), normal (m) and binormal (b) directions, m pointing into the material side. r *and* θ are the polar coordinates in the normal plane (m,b). The asymptotic distribution of the normal stress and displacement components at point P can be expressed as

$$\sigma_{bb}(r,\theta) = \frac{K_I(s)}{\sqrt{2\pi r}} \cos\left(\frac{\theta}{2}\right)\left[1 + \sin\left(\frac{\theta}{2}\right)\sin\left(\frac{3\theta}{2}\right)\right] \tag{2.1}$$

$$u_b(r,\theta) = \frac{1+\nu^P}{E^P}\sqrt{\frac{2r}{\pi}}K_I(s)\sin\left(\frac{\theta}{2}\right)\left[2\left(1-\nu^P\right)-\cos^2\left(\frac{\theta}{2}\right)\right] \tag{2.2}$$

In these equations P stands for the material properties at the crack tip. In order to calculate the mode I stress intensity factors, a section at point P parallel to the normal plane (n, b) is taken (Figure 2.2). The nodes 1, 2 and 3 are on the edge of a collapsed 20 – node brick element (Figure 2.3).

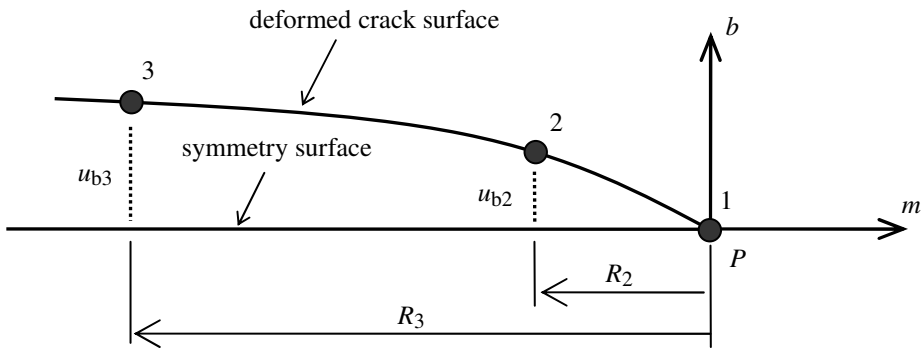

Figure 2.2. Deformed shape of the crack surface and point P on the crack front [15]

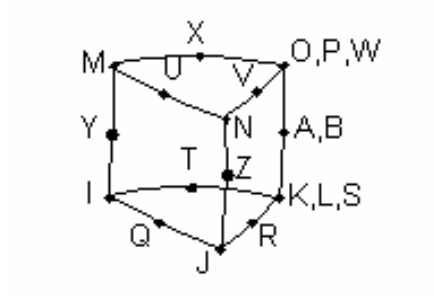

Figure 2.3. Collapsed 20 node brick element

Using equation (2.2), the displacement field on the crack surface ($\theta = \pi$) can be written as

$$u_b(r,\pi) = \frac{4(1-\nu^{P2})}{E^P}\left(\sqrt{\frac{r}{2\pi}}\right)K_I \tag{2.3}$$

The mode I stress intensity factor can now be expressed as

$$K_I = \frac{\sqrt{2\pi}E^P}{4\left(1-\left(\nu^P\right)^2\right)}\left[\lim_{r\to 0}\left\{\frac{u_b(r,\pi)}{\sqrt{r}}\right\}\right] \tag{2.4}$$

Now the limit gives 0/0 undefined case near the crack tip as r goes to zero. The convenient way is using the linear extrapolation technique to evaluate $\frac{u_b(r,\pi)}{\sqrt{r}}$ part of equation (2.4).

$$\frac{u_b(r,\pi)}{\sqrt{r}} \cong Ar + B \tag{2.5}$$

Two boundary conditions are necessary to evaluate the first order expression given in equation (2.5). These are

Point 1: when $r = R_2$, $u_b = u_{b2}$

Point 2: when $r = R_1$, $u_b = u_{b1}$

$$r = R_2 \rightarrow \frac{u_b(R_2,\pi)}{\sqrt{R_2}} = \frac{u_{b2}}{\sqrt{R_2}} = AR_2 + B \tag{2.6}$$

$$r = R_3 \rightarrow \frac{u_b(R_3,\pi)}{\sqrt{R_3}} = \frac{u_{b3}}{\sqrt{R_3}} = AR_3 + B \tag{2.7}$$

In equations (2.6) and (2.7), the unknowns are A and B, and they are found as

$$A = \frac{\sqrt{R_2}u_{b3} - \sqrt{R_3}u_{b2}}{\sqrt{R_2}\sqrt{R_3}(R_3 - R_2)} \tag{2.8}$$

$$B = \frac{R_3^{3/2}u_{b2} - R_2^{3/2}u_{b3}}{\sqrt{R_2}\sqrt{R_3}(R_3 - R_2)} \tag{2.9}$$

The A value vanishes at the crack tip if r value is very small. So the $\frac{u_b(r,\pi)}{\sqrt{r}}$ expression will be equal to B as r→0. Therefore equation (2.4) takes the form below.

$$K_I = \frac{\sqrt{2\pi}E^P}{4\left(1-\left(\nu^P\right)^2\right)}B \tag{2.10}$$

Using equations (2.9) and (2.10), stress intensity factor K_I can now be expressed as below.

$$K_I = \frac{\sqrt{2\pi}E^P}{4\left(1-\left(\nu^P\right)^2\right)}\left[\frac{R_3^{3/2}u_{b2} - R_2^{3/2}u_{b3}}{\sqrt{R_2}\sqrt{R_3}\left(R_3 - R_2\right)}\right] \tag{2.11}$$

The mode I stress intensity factors around the crack front can now be calculated provided that the displacement field is solved using the finite element method. Note that equation (2.11) is valid for both three dimensional and plane strain problems.

2.2 Verification of Displacement Correlation Technique for FGMs

Equation (2.11) is validated for FGMs by finite element modeling of a plane strain surface crack under mode I loading. The problem geometry is given in Figure 2.4. This is the case investigated for different crack lengths (*b*) by Kadioglu *et al.* [23] and Guo *et al.* [24]. The crack is loaded by applying normal stress to its surfaces. Variation of the normal stress is given by the equation $\sigma_{yy}(x) = \sigma_0 \exp(\beta x)$. The variation function of the modulus of elasticity is given as $E(x) = E_c \exp(\beta x)$. In these expressions, constant β shows the characteristic property of FGM material with the expression, $\beta = \dfrac{\ln(E_m / E_c)}{H}$ and it is taken as ln(10)/*H*. The subscripts *c* and *m* refer to ceramic and metal, respectively. Poisson's ratio is taken as constant in this problem. A model is created by writing an APDL source code. APDL stands for ANSYS Parametric Design Language, a scripting language that can be used to automate tasks and build the model in terms of parameters (variables). It also provides a wide range of other features such as repeating a command, macros, if-then-else branching, do-loops, and scalar, vector and matrix operations.

2.2.1 Finite Element Modeling of the Surface Crack

The finite element model is generated by the use of modeling method of fracture mechanics problems in ANSYS explained in [25]. The created model is shown in Figure 2.5 with the meshed structure. Symmetry boundary condition is given to the line where there is no crack. This line represents the line of symmetry. The displacement perpendicular to this line is fixed. Loading function $\sigma_{yy}(x)$ is applied on the crack surface.

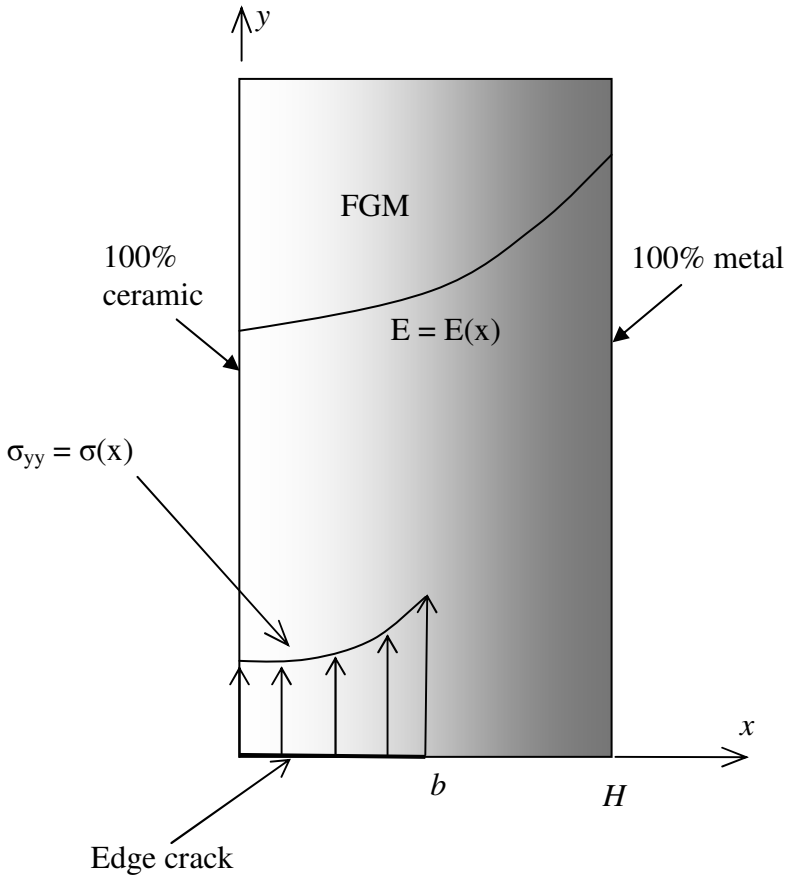

Figure 2.4. FGM model with surface crack

In the generation of the mesh structure Plane82 plane strain elements are used (Figure 2.6). Plane82 is an 8-node element with quadratic shape functions and has two degrees of freedom at each node: translations in the nodal *x* and *y* directions [26]. While generating the mesh structure the effort was to prevent distorted elements. In that case ANSYS gives errors for the elements that violate shape warning limits. The meshing structure at the crack tip is very important for the calculation of stress intensity factors so a special meshing technique of ANSYS is used to generate concentrated mesh structure at the crack tip. The command parameters are adjusted to use quarter point elements at the crack tip. The other parts of the mesh do not influence the results significantly but in order to eliminate

the error messages, appropriate divisions are given to minimize the number of distorted elements.

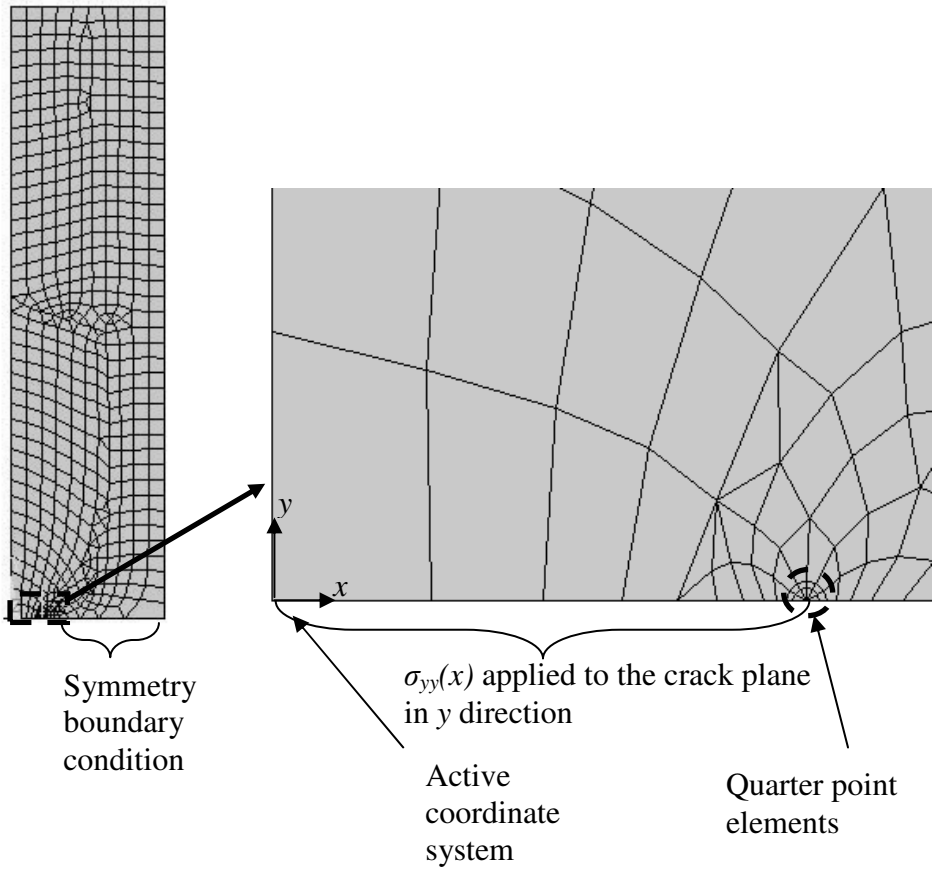

Figure 2.5. Mesh structure of surface crack model with applied boundary conditions

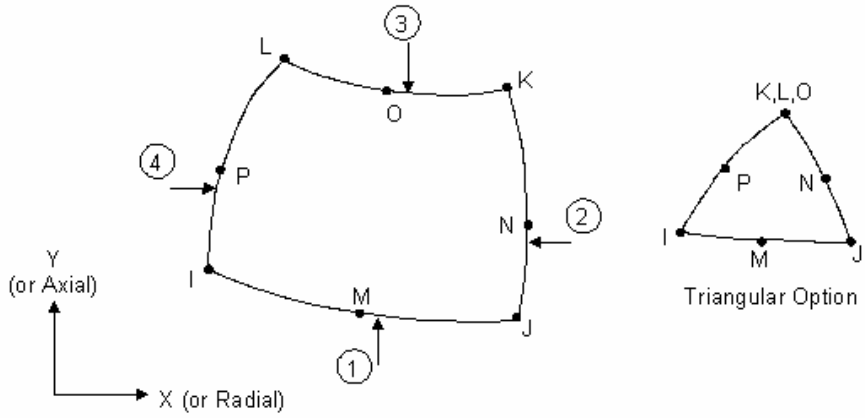

Figure 2.6. Plane 82 Element [26]

2.2.2 Application of Material Properties

The material properties are assigned according to variation function by using the centroidal coordinates of each element. The procedure is applied by running loops from the initial element number to the final one. At each cycle, the *x*-coordinate of the centroid of the element is inserted into the expression of variation function of material properties. By this way each element has unique material property according to its position. After the assignment of material properties, the analysis is ready to be run.

2.2.3 Post Processing and Application of the Displacement Correlation Technique

For the application of displacement correlation technique, the two nodes of the element at the crack tip are used. As it is discussed, the vertical displacements of the nodes will be used to calculate the stress intensity factors. Figure 2.7 shows the crack tip region after the analysis. The triangular elements at the crack tip are the

quarter point elements. The distance between the interior node and the crack tip node is ¼ times the distance between the outer node and the crack tip node. Note that the displacements of the nodes are exaggerated in this view.

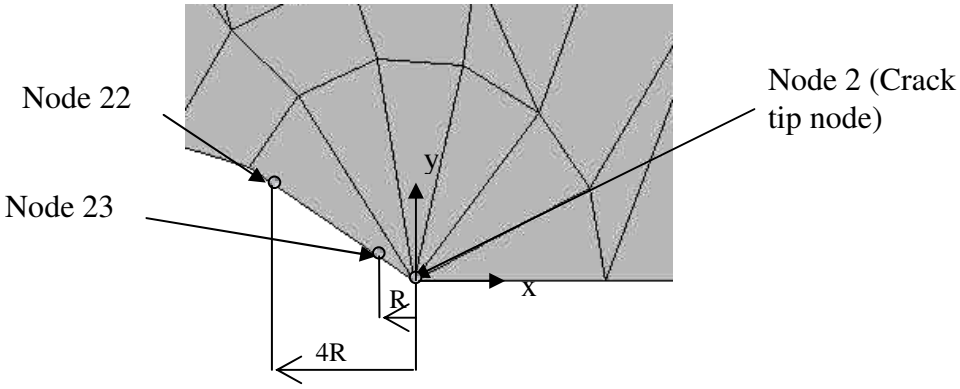

Figure 2.7. Crack tip region after the solution is obtained

First of all, a local coordinate system is defined at the crack tip with the x axis on the symmetry line. The initial *x*-coordinate and *y*-displacement of nodes 22 and 23 are taken as inputs for the calculation. Then equation (2.11) is used to calculate the stress intensity factor at the crack tip.

The stress intensity factors are evaluated for different *b/H* ratios and normalized as $f = K_I / \sqrt{\pi a}$. By this way it will be possible to check the validity of the present results by comparing to those given in [23] and [24].

2.2.4 Results and Discussions

The results are presented in Table 2.1 for different *a/H* ratios. It is seen that the calculated values are very close to those given in the mentioned references. From this analysis, it can be said that displacement correlation technique is a suitable way of determining the stress intensity factor for FGM structures.

Table 2.1. Normalized SIFs for edge crack

a/H	***Present Study***	***Kadioglu et al. [23]***	***Difference %***	***Guo et al. [24]***	***Difference %***
0.1	1.261	1.274	1.020	1.268	0.549
0.2	1.590	1.582	0.506	1.580	0.632
0.4	2.899	2.895	0.138	2.911	0.415
0.5	4.225	4.259	0.798	4.285	1.409
0.6	6.709	6.747	0.563	6.783	1.097

CHAPTER 3

FATIGUE AND FRACTURE MECHANICS

3.1 Fatigue Failure

Fatigue failure occurs in structures when variable loads are applied on them. This type of loading is very common. For example, rotating shafts and pistons or wave-impact on oil rigs cause cyclic, variable loads. Vibration can also cause quite large, high frequency, variable loads.

The frequency of the cyclic variable load is not very important. The fatigue life is the number of load cycles that will cause failure. It can vary between a few thousand to hundreds of millions of cycles, with longer lives at lower loads.

Fatigue failure is due to the nucleation and growth of fatigue cracks. The crack grows by a small amount each cycle, producing characteristic fatigue markings on the fracture surface. These markings can be seen on the fracture surface at the highest magnification [27].

Figure 3.1 is an image from an aluminum alloy forging which failed by fatigue after some time in service. The bands which run almost horizontally across the lower magnification image are the cracked regions. These cracks occur on the fracture surface at different times during the lifetime of the forging and develop when the amplitude of the cyclic variable load changes. The crack extensions therefore record the history of the component's service.

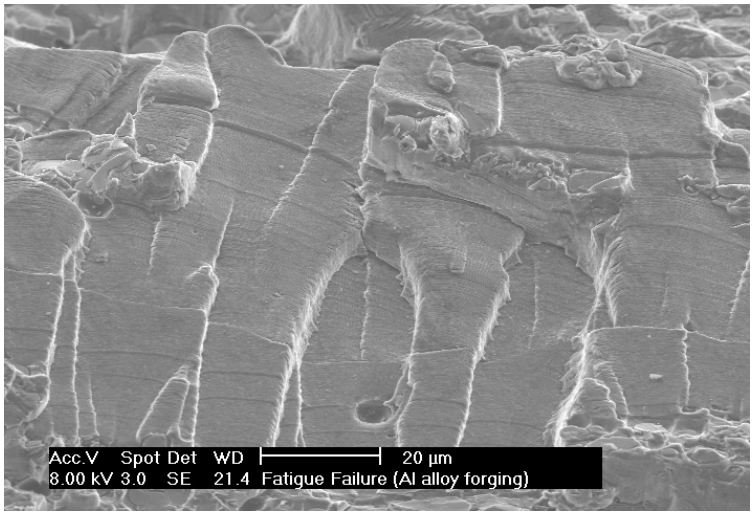

Figure 3.1. Cracks on aluminum alloy forging [27]

3.2 Fatigue Crack Growth

Fatigue failure can occur at quite low loads, and this leads to employment of the principles of linear elastic fracture mechanics to provide data for strength analysis of cracked or flawed structures or components. Even though the advancement of crack is a fully plastic phenomenon, low values of load leads to the implementation of the theory of elasticity. Many efforts have been made for the crack growth behavior of materials throughout the history. Note that all the theories of fatigue with fracture mechanics studies assume that a crack is always present. Otherwise, the principles of linear elastic fracture mechanics cannot be applied.

One of the aims of these efforts is to predict the number of cycles spent in growing a crack to some specified length or to final failure by applying fracture mechanics principles. Typical constant amplitude crack propagation data are shown in Figure 3.2. The crack length, a, is plotted versus the corresponding number of cycles, N, at which the crack was measured [28].

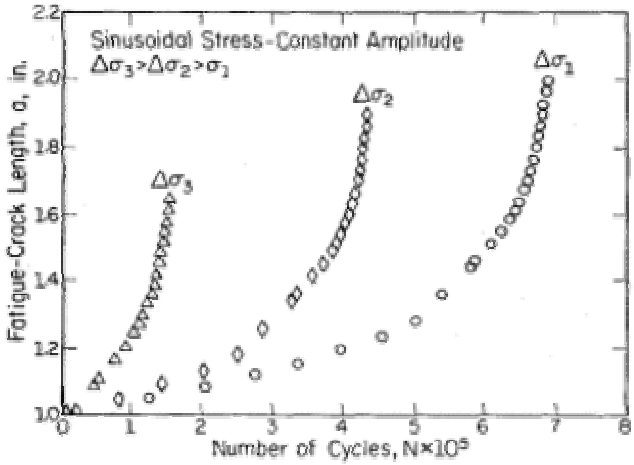

Figure 3.2. Constant amplitude crack growth data [28]

As it can be seen from the figure, most of the life of the component is spent while the crack length is relatively small. In addition, the crack growth rate increases with increased applied stress. The crack growth rate, *da/dN*, is obtained by taking the derivative of the above crack length, a, with respect to *N*. A plot of log(*da/dN)* versus log*(ΔK)* can be obtained as shown in Figure 3.3. This curve may be divided into three regions.

At low stress intensities, crack behavior is associated with a threshold stress intensity value, K_{th}, below which fatigue crack growth is negligible. This is seen in the first region of the figure.

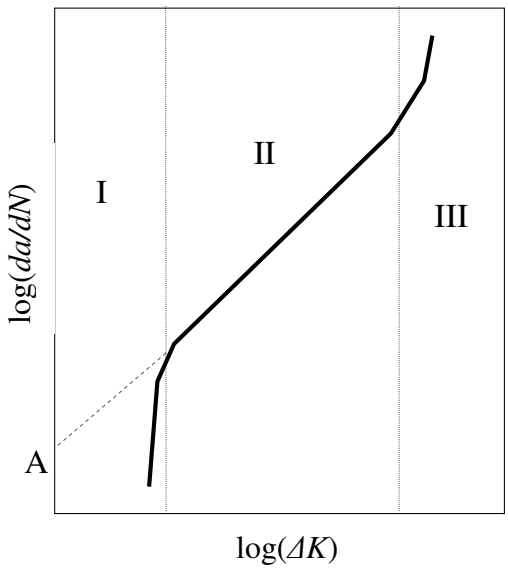

Figure 3.3. Fatigue crack growth behavior of materials [29]

In the second region of stress intensities, the log(*da/dN)* versus log*(ΔK)* curve is essentially linear with a slope. Most structures operate in this region. Most of the current applications of linear elastic fracture mechanics (LEFM) concepts used to describe fatigue crack growth behavior are associated with Region II.

Region II is generally the largest region of the fatigue crack growth rate curve and many curve fits for this region have been suggested. The Paris and Erdoğan formulation (commonly referred to as the Paris Equation or Paris' Law), which was proposed in 1963, is the most widely accepted equation for region II crack growth of materials [30]. The equation is,

$$\frac{da}{dN} = C\Delta K^{n} \tag{3.1}$$

Here, *da/dN* is the crack growth rate. *C* and *n* are Paris-Erdoğan law constant and exponent, respectively. The values of *C* and *n* can be found in literature or by

performing fatigue crack growth tests as given in ASTM E399. ΔK is the difference between minimum and maximum stress intensity factors existed in the cycle.

Although this law is first developed for the fatigue crack growth behavior of metals, it can also be used for the ceramics. However, compared to typical values of between 2 and 4 for most metals, the Paris-Erdoğan law exponent can take the values as high as 50 in ceramics [31]. In Chapter 4, the 2D models of three standard specimens given in ASTM E399 are analyzed using Paris-Erdoğan equation.

At high stress intensities, crack growth rates are extremely high and little fatigue life is involved. Region III is characterized by rapid, unstable crack growth. The crack growth rate accelerates as the maximum stress intensity factor approaches the fracture toughness of the material. In many practical engineering situations this region may be ignored because it does not affect the total crack propagation life. The point of transition from Region II and Region III behavior is dependent on the yield strength of the material, stress intensity factor, and stress ratio [32].

3.3 Fracture Toughness

As the stress intensity factor reaches a critical value, unstable fracture occurs. This critical value of the stress intensity factor is known as the fracture toughness of the material. The fracture toughness can be considered as the limiting value of stress intensity just as the yield stress might be considered the limiting value of applied stress. If a material has a large value of fracture toughness it will probably undergo ductile fracture. Brittle fracture is very characteristic of materials with a low fracture toughness value. The former case represents the fracture behavior of metals whereas the latter is for the ceramic materials' fracture when this critical stress intensity factor value is reached [28]. The material's thickness is related to its fracture toughness and this behavior is given in Figure 3.4.

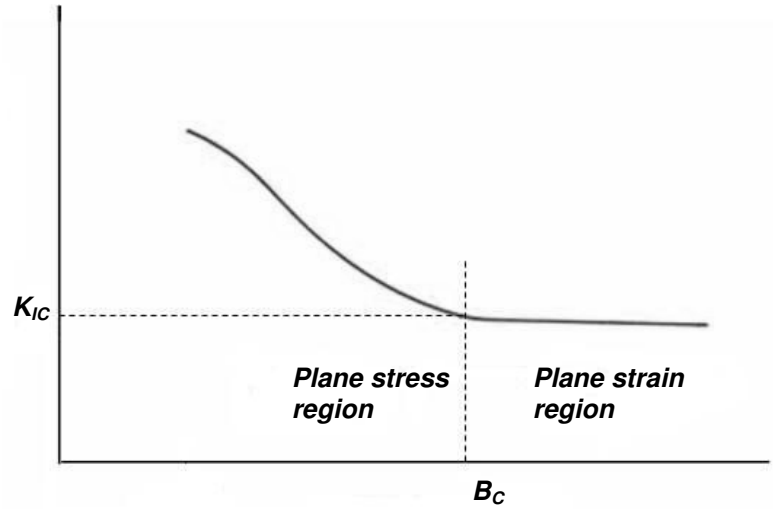

Figure 3.4. Fracture toughness as a function of material thickness [29]

There are actually four different types of fracture toughness, K_C, K_{IC}, K_{IIC}, and K_{IIIC}. K_C is used to measure a material's fracture toughness in a sample that has a thickness less than B_C and its value is given in equation (3.2).

$$B_C = 2.5\left(\frac{K_{IC}}{\sigma_y}\right) \tag{3.2}$$

When the material's thickness is less than B_C, and stress is applied, the material is in a plane stress state. K_{IC}, K_{IIC}, and K_{IIIC} all represent a material's fracture toughness when the thickness is greater than B_C and this state is called the plane strain state. These values are the fracture toughness of a material under the three different modes of fracture, mode I, mode II, and mode III, respectively (Figure 3.5) [33].

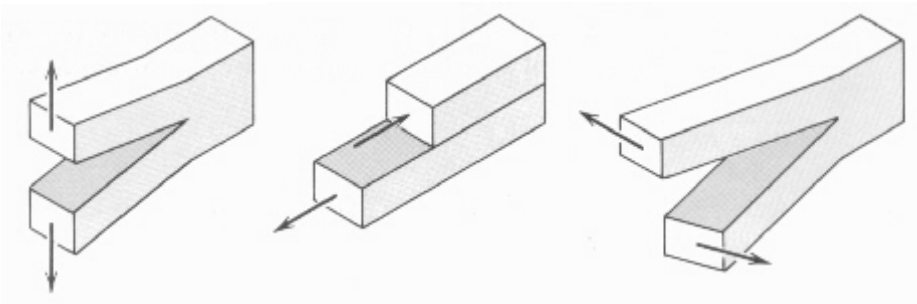

(a) (b) (c)

Figure 3.5. The fracture modes (a, b, c; mode I, II and III respectively) [33].

This study includes the loading case mode I so K_{IC} values will be used to determine critical crack lengths for the applied stress.

The K_{IC} values of materials are determined by ASTM Designation E399, Standard Method of Testing for Plane Strain Fracture Toughness of Metallic Materials. This standard sets forth accepted procedures for determining this value. Some of the common metal and ceramic materials' fracture toughness values at room temperature are given in Table 3.1.

Table 3.1 K_{IC} values of some metal and ceramic materials [34,35,36,37]

Metal	$K_{IC}\,(MPa\sqrt{m})$	***Ceramic***	$K_{IC}\,(MPa\sqrt{m})$
Aluminum 7075	16-41	Zirconia	5
Ti-6Al-4V	75	Si_3N_4	6-6.5
Mild Steel	140	Al_2O_3	2.9-3.4
High Strength Steel	50-154	Soda-lime-glass	0.6-1.2

As it is seen in the table, the ceramic materials have a much lower K_{IC} value than the metals. The low K_{IC} value reflects the fact that ceramic materials are very susceptible to cracks and undergo brittle fracture whereas the metals undergo ductile fracture.

It should also be noted that K_{IC} values are highly dependent on material temperature. As the usual use of FGMs are high in temperature applications, this must also be considered in the design of FGMs against fracture.

CHAPTER 4

CRACK GROWTH ANALYSIS OF STANDARD FGM TEST SPECIMENS

4.1 Test Specimens of ASTM E399

In the first part of the study, three of the standard specimen geometries are studied which are given in ASTM E399, "Plane-Strain Fracture Toughness of Metallic Materials" [38]. The geometries have been certified for K_{IC} testing. The size and shape of these specimens are selected according to the needs established by fracture-testing community and the availability of accurate stress intensity factor calibrations.

In the standard ASTM E399, it was mentioned that, the fatigue crack growth test procedure should be carried out by loading the test specimens in tension or three-point bending. Load versus displacement across the notch at the specimen edge is recorded autographically. The load corresponding to a 2% apparent increment of crack extension is established by a specified deviation from the linear portion of the record.

Given in the standard, in all of the specimens, B, which is the specimen thickness, is between 0.45 and 0.55 times the width, W. The ratio W/B is nominally equal to two.

The standard specimen geometries that are analyzed in this study are bend bar specimen, compact specimen and arc bend specimen

4.1.1 Bend Bar Specimen

The standard bend bar specimen is a single edge notched cracked beam loaded in three-point bending with a support span, *S*, nominally equal to four times the width, *W*. The general proportions of this specimen configuration are shown in Figure 4.1

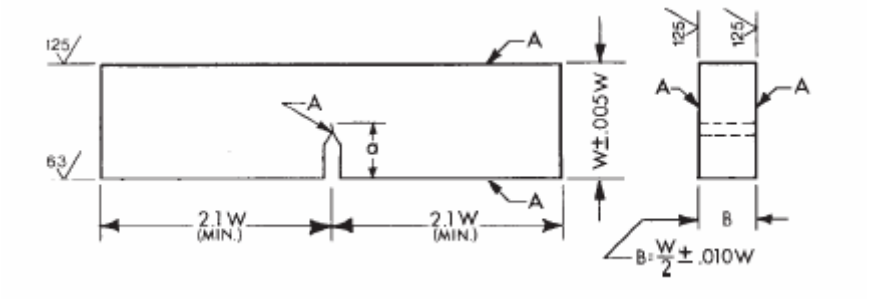

Figure 4.1. Bend bar specimen – standard proportions and tolerances ("A" surfaces should be perpendicular within 0.001 TIR) [38]

In order to carry out the static or fatigue crack growth testing bend test fixture is required to test this specimen. The general configuration of the fixture is illustrated in Figure 4.2. This fixture is designed to minimize frictional effects by allowing the support rollers to rotate and move apart slightly as the specimen is loaded, thus permitting rolling contact. The support rollers are allowed limited motion along plane surfaces parallel to the notched side of the specimen, but are initially positively positioned against stops that set the span length and are held in place by low-tension springs.

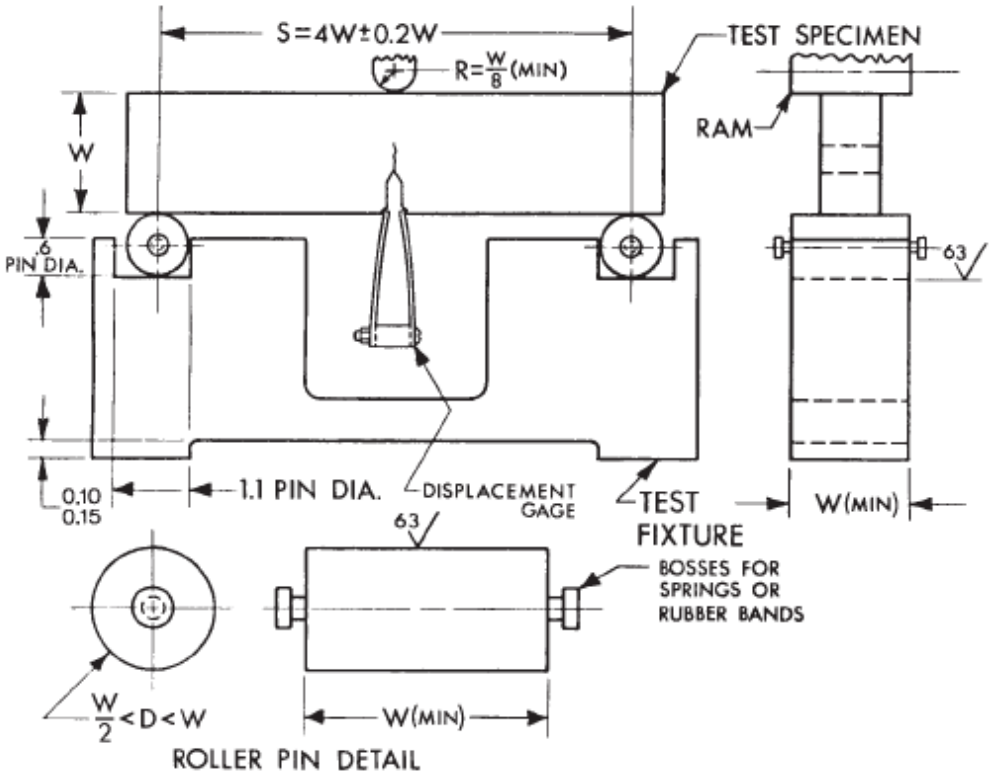

Figure 4.2. Bend-bar test fixture design [38]

Before the test, the test fixture is set up so that the line of action of the applied load and the crack tip position shall pass midway between the support roll centers. The displacement gage is seated on the knife edges to maintain registry between knife edges and gage grooves.

4.1.2 Compact Specimen

The standard compact specimen is a single edge notched cracked plate loaded in tension. The general proportions of this specimen configuration are shown in Figure 4.3. This specimen is used when the geometry of the sample that the specimen is taken out is not large enough to create bend bar specimen

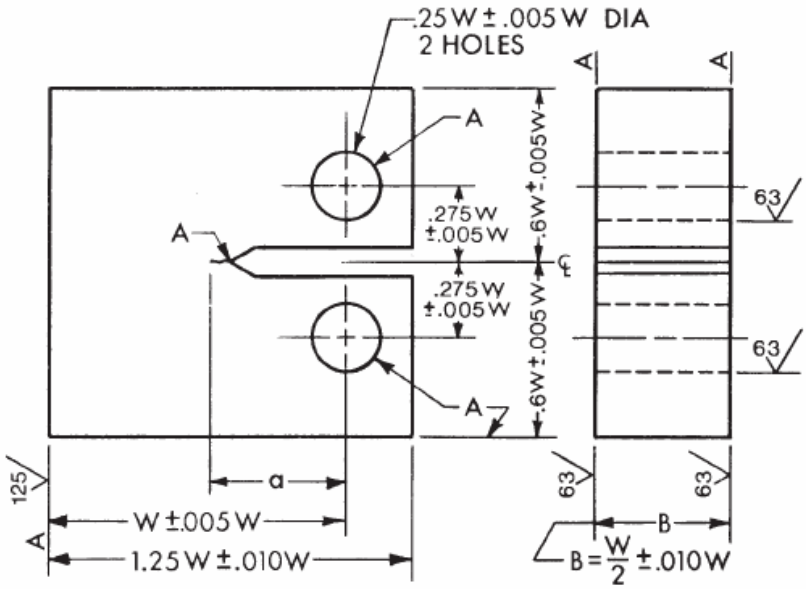

Figure 4.3. Compact specimen standard proportions and tolerances [38]

The specimen can be loaded to a standard tensile test device by using a connection fixture which is called the clevis. With this fixture, both ends of the specimen are held in and loaded through pins in order to allow rotation of the specimen during testing.

4.1.3 Arc Bend Specimen

The arc shaped tension specimen is a single edge notched cracked ring segment loaded in tension. This specimen is used if the sample is circular shaped. The general proportions of the specimen are shown in Figure 4.4. The value of the radius ratio r_1/r_2 is not specified, so that specimens can be taken out from any cylindrical geometry. A similar clevis used in compact specimen can also be used for arc bend specimen

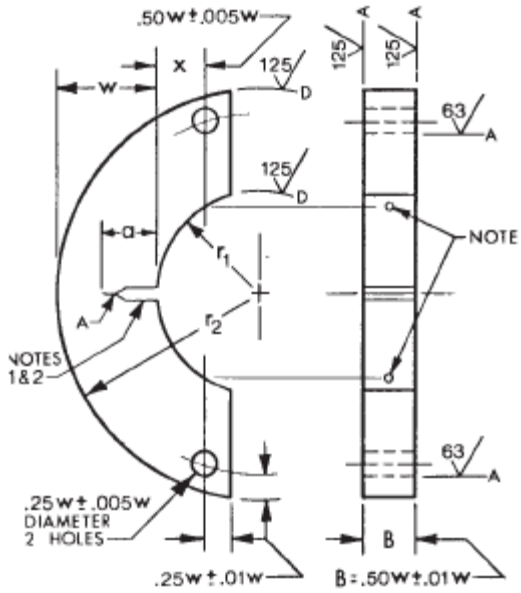

Figure 4.4. Arc bend specimen standard proportions and tolerances [38]

4.2 Parametric Modeling of FGM Test Specimens

Before the analysis of fatigue crack growth, stress intensity factors of test specimens with different variations of metal and ceramic materials should be determined according to the crack length. By using an APDL code, geometries are modeled with different crack lengths and material variations.

The APDL codes are prepared according to the dimensions given in ASTM standard E399. The width of the specimens (*W*) is taken as 40mm and inner radius (r_1) and outer radius (r_2) are taken as 40mm and 80mm, respectively, for arc bend specimen. The thickness to width ratio (*a/W*) is given as between 0.45 and 0.95 for the modeling of different crack lengths. In the standard, the geometry of the notch opening at the crack plane is not given so an assumption is made for the dimensions of this region.

4.2.1 Finite Element Modeling of Bend Bar Specimen

Finite element models of specimens are created by first dividing the lines of the specimens so that equally shaped meshed structure can be created. The command parameters are adjusted to generate 12 quarter point elements at the crack tip. The mesh structure of the geometry is given in Figure 4.5.

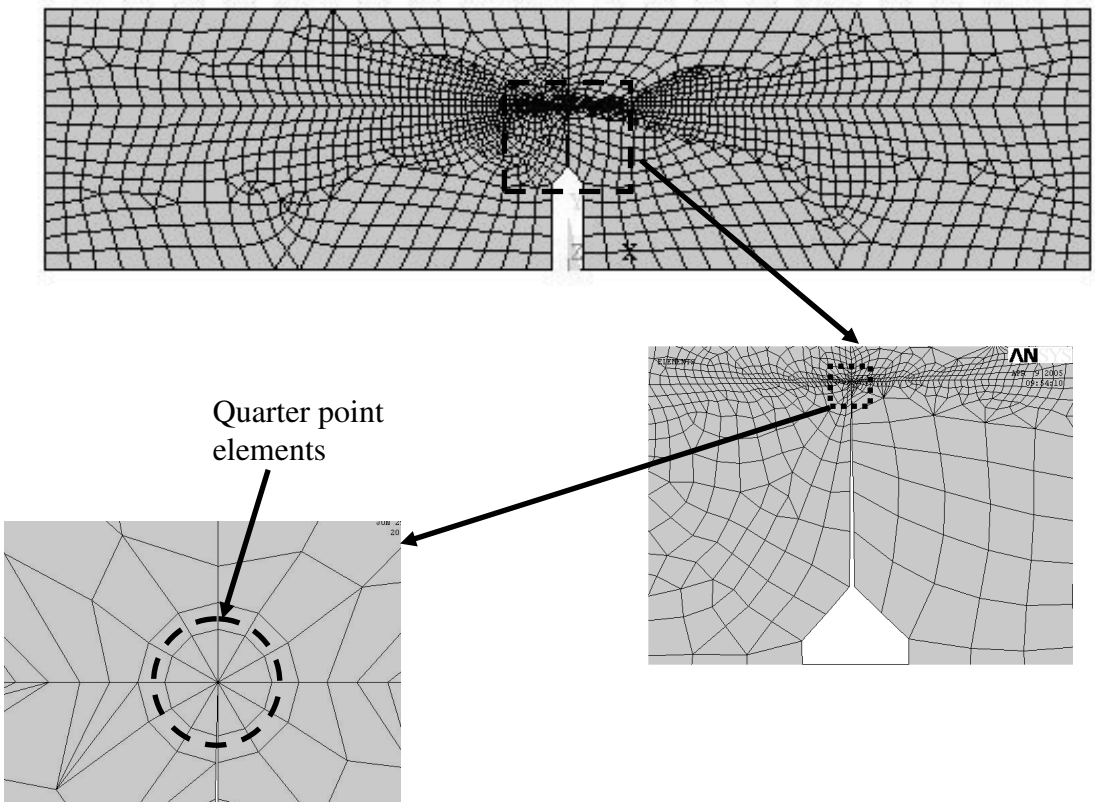

Figure 4.5. Mesh structure of bend bar specimen

Upon investigation of Figure 4.2, it is observed that the test specimen is mounted on two rollers resembling a simply supported beam. These rollers are free to move so that pure bending condition is satisfied on the test specimen. In the analyses,

boundary condition is given as fixing the displacements at the roller points in vertical direction and fixing the horizontal displacement of one of the rollers to prevent the motion of the model. By this way, the deformation in x direction is allowed for free bending. The pressure applied by the upper roller is given as concentrated load in the finite element model as shown in Figure 4.6

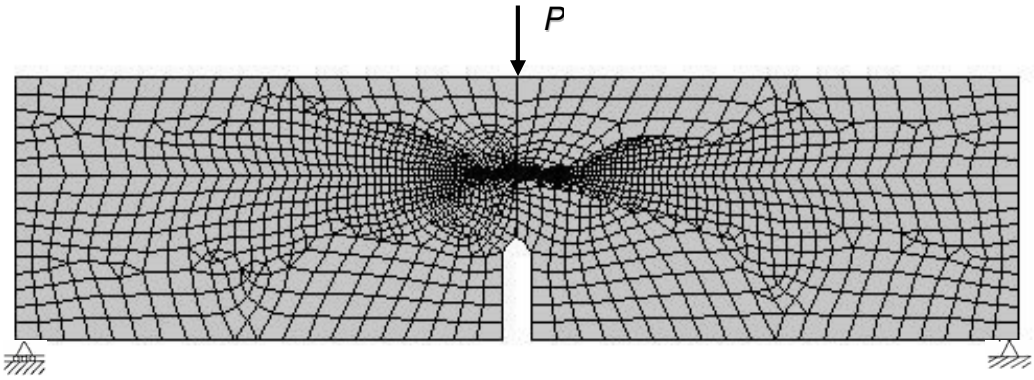

Figure 4.6. Supports and the applied load for the bend bar specimen

4.2.2 Finite Element Modeling of Compact Specimen

In this geometry, the boundary conditions and the model are symmetric with respect to mid-axis. So only one half of the geometry is modeled and analyses are carried out by using the symmetry conditions at the mid line of the specimen. The meshed structure of compact specimen is given in Figure 4.7.

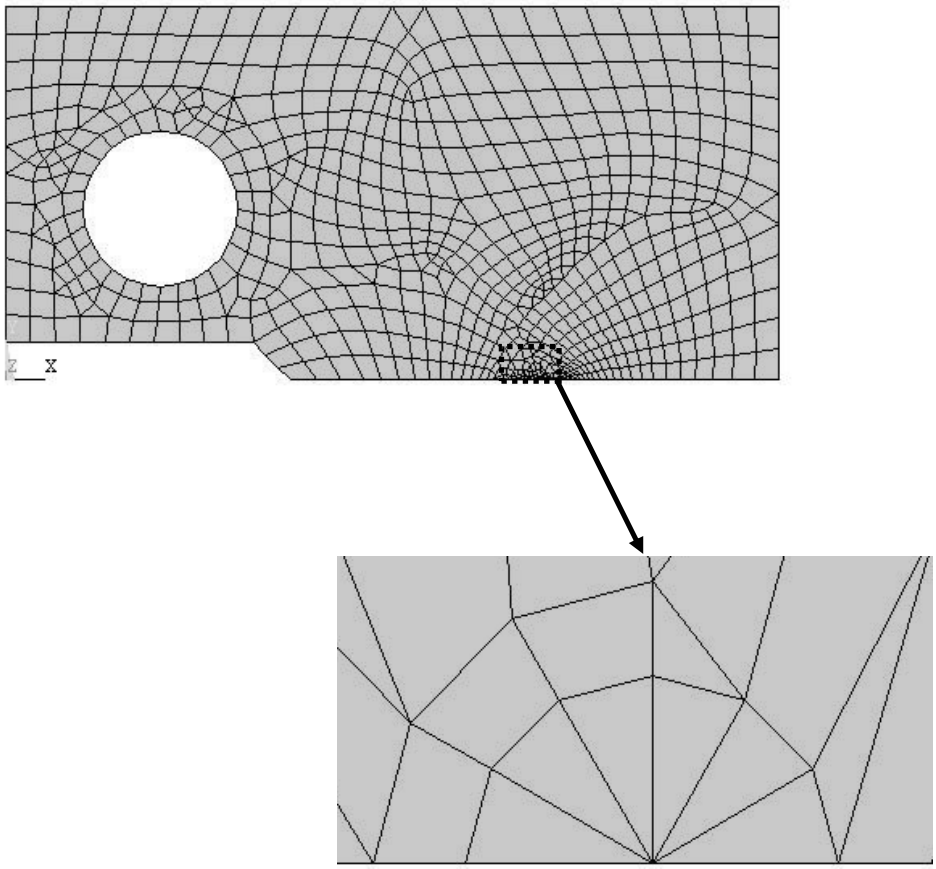

Figure 4.7. Mesh structure of compact specimen

Unit load is applied to the upper keypoint of the hole and symmetry condition is applied to the no-crack side of the specimen. In the real test, the specimen is pulled upwards with a fixture as discussed before creating distributed loading condition at the upper side of the hole. But the analyses with concentrated load gave highly accurate results. This gave the opportunity of application of concentrated load to the model shown in Figure 4.8.

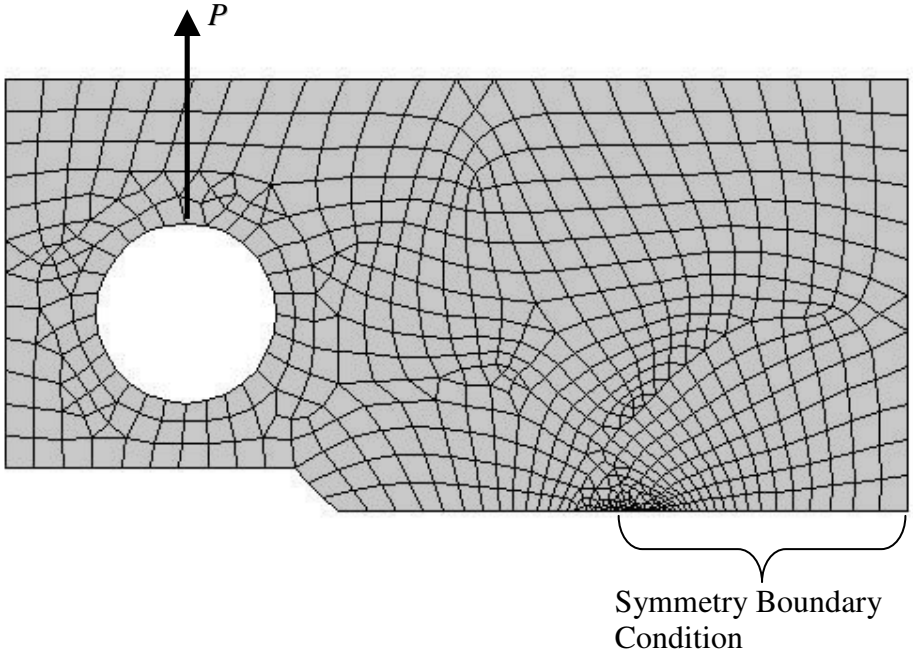

Figure 4.8. Boundary conditions of compact specimen

4.2.3 Finite Element Modeling of Arc Bend Specimen

The modeling procedure of arc bend specimen is about the same as compact specimen. Again there is the application of symmetry conditions at the line of symmetry and point load is applied at the holes. The mesh structure with the boundary conditions are given in Figure 4.9

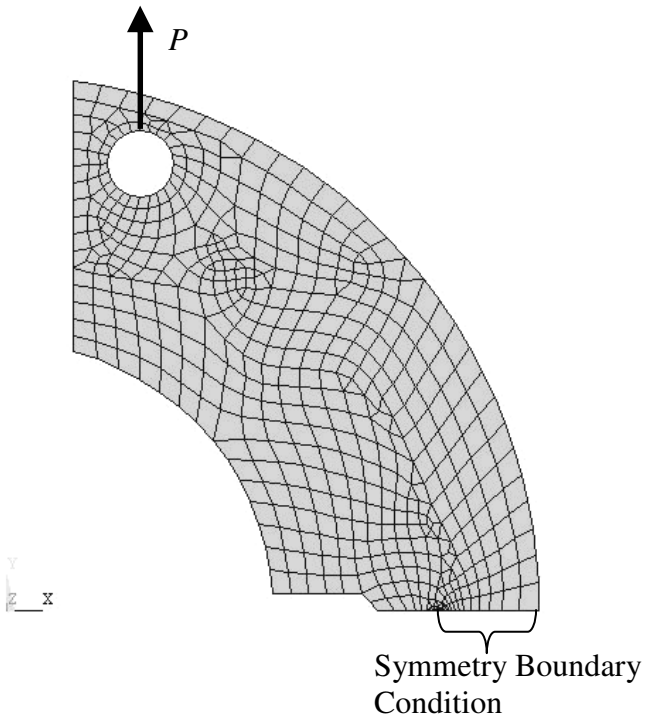

Figure 4.9. Mesh structure and boundary conditions of arc bend specimen

4.3 Specimen Material Properties

4.3.1 The materials used in the study

In the analysis of the fatigue crack growth, the ceramic and metal components of the functionally graded material are taken as zirconia (ZrO_2) and titanium alloy (Ti-6Al-4V), respectively.

Properties of Zirconia (ZrO_2)

Zirconia, exists as a monoclinic crystal at room temperature inverting to tetragonal phase above approximately 1200℃. The addition of large amounts of a stabilizer such as magnesium oxide or yttrium will induce a cubic crystal structure during firing that does not revert to the monoclinic phase upon cooling. The addition of generally less than 10% by weight of stabilizers yields high-density ceramic bodies known as transformation toughened zirconia.

Zirconia is stable in oxidizing and mildly reducing atmospheres. It reacts with carbon, nitrogen and hydrogen at temperatures above 2200℃. It is inert to acids and bases at room temperature and does not react with the refractory metals up to 1400℃ [39]. The high temperature resistence of zirconia and relatively high strength among the ceramics makes it a perfect ceramic material for FGMs.

Pure zirconia is an oxide which cannot be obtained at room temperature without being damaged by distributed microcracks due to phase transformations occurring during the cooling process. For this reason pure zirconia is not used as a structural material. A stabilization of the cubic phase during the cooling process, by means of doping with calcia (CaO), magnesia (MgO), yttria (Y_2O_3) or ceria (CeO_2) can provide a material which does not exhibit damage or smeared cracks at room temperature. The material considered in this study is a yttria doped tetragonal zirconia polycrystal (TZP) [40].

Properties of Ti-6Al-4V

One of the most commonly used titanium alloys is an alpha-beta alloy containing 6% Al and 4% V. This alloy exhibits an excellent combination of corrosion resistance, strength and toughness. Typical uses include medical devices or implants, aerospace applications and pressure vessels. The interstitial elements of

iron and oxygen are carefully controlled to improve ductility and fracture toughness [41].

Ti-6Al-4V is widely used in turbine blades because of its corrosion resistance. To protect from high temperature, the blades are coated with a ceramic or FGM material.
The material properties of these materials are given in Table 4.1

Table 4.1. Material Properties of Zirconia and Ti-6Al-4V [15]

Component	***E [GPa]***	***ν***
ZrO_2	116.46	0.333
Ti-6Al-4V	105.8	0.298

4.3.2 Variation of Material Properties

The material properties are varying across the thickness according to the variation function in functionally graded materials as discussed in Chapter 1. The variation function for modulus of elasticity and Poisson ratio are given individually for different type of specimens to simulate the realistic models. Figure 4.10 shows the specimen models with the coordinate system.

For bend bar specimen (Figure 4.10a) the material thickness direction is given along *y* axis. The variation function for this type of specimen is given as

$$E(y) = E_c + (E_m - E_c)(y/W)^p \tag{4.1}$$

$$\nu(y) = \nu_c + (\nu_m - \nu_c)(y/W)^p \tag{4.2}$$

For compact specimen (Figure 4.10b), the variation is given along x axis with the total material thickness given as $1.25W$. So equations (4.1) and (4.2) are modified for this specimen and given as equations (4.3) and (4.4).

$$E(x) = E_c + (E_m - E_c)(x/1.25W)^p \tag{4.3}$$

$$\nu(x) = \nu_c + (\nu_m - \nu_c)(x/1.25W)^p \tag{4.4}$$

In arc bend specimen (Figure 4.10c), the variation function is defined according to cylindrical coordinates and given as equations (4.5) and (4.6). This model can represent an internal coating. Here, r_1 is the radial coordinate of the 100% ceramic surface (inner radius), and r_2 is the radial coordinate of the 100% metal surface (outer radius).

$$E(r) = E_c + (E_m - E_c)[(r - r_1)/(r_2 - r_1)]^p \tag{4.5}$$

$$\nu(r) = \nu_c + (\nu_m - \nu_c)[(r - r_1)/(r_2 - r_1)]^p \tag{4.6}$$

In equations (4.1) through (4.6), parameter p defines the coating type of FGM structure which are given in Table 4.2. Figure 4.11 shows the variation of the modulus of elasticity values of the FGM along the thickness for different p values. When p value is large, the material gets closer to the homogeneous ceramic case whereas small p values improve the metal content.

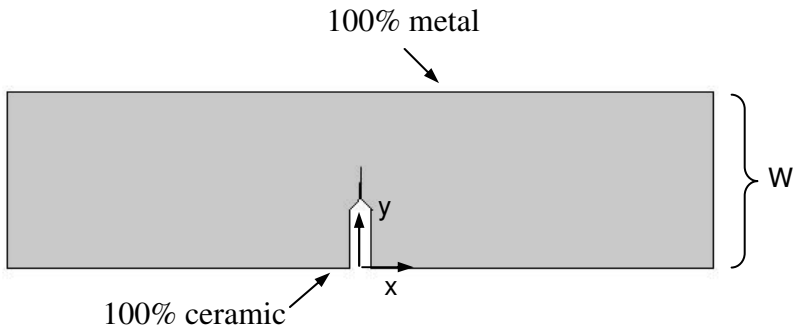

(a)

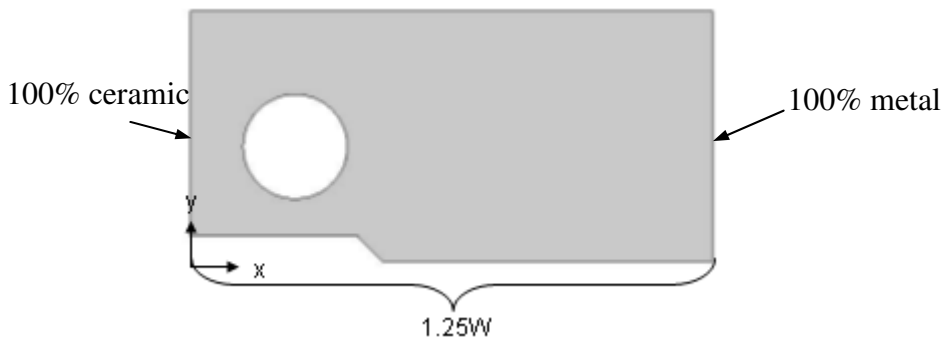

(b)

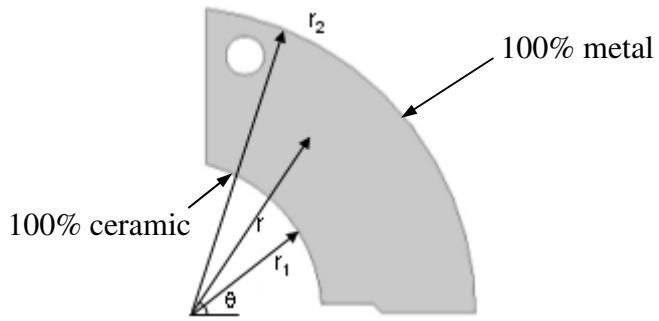

(c)

Figure 4.10. Coordinate systems for (a) bend bar specimen, (b) compact specimen, (c) arc bend specimen

Table 4.2. The values of the exponent p and the corresponding material property variation types

Coating Type	***Homogeneous ceramic (HC)***	***Ceramic – rich (CR)***	***Metal – rich (MR)***	***Linear variation (LN)***
p	∞	5	0.2	1

4.4 Calculated Stress Intensity Factors

The non-dimensional stress intensity factors are calculated according to different *a/W* ratios of the crack tip. The results are also compared to the equations given in the standard ASTM E399 to see the applicability of displacement correlation technique. The results are non-dimensionalized by the equations given in the explanation of each table [42].

Bend Bar Specimen

For the standard bend bar specimen the provisional stress intensity factor is computed from

$$K_I = \frac{P}{BW^{1/2}} . f\left(\frac{a}{W}\right) \tag{4.7}$$

where,

$$f\left(\frac{a}{W}\right) = \frac{\left(2+\frac{a}{W}\right)\left(0.886+4.64\frac{a}{W}-13.32\left(\frac{a}{W}\right)^2+14.72\left(\frac{a}{W}\right)^3-5.6\left(\frac{a}{W}\right)^4\right)}{\left(1-\frac{a}{W}\right)^{3/2}} \tag{4.8}$$

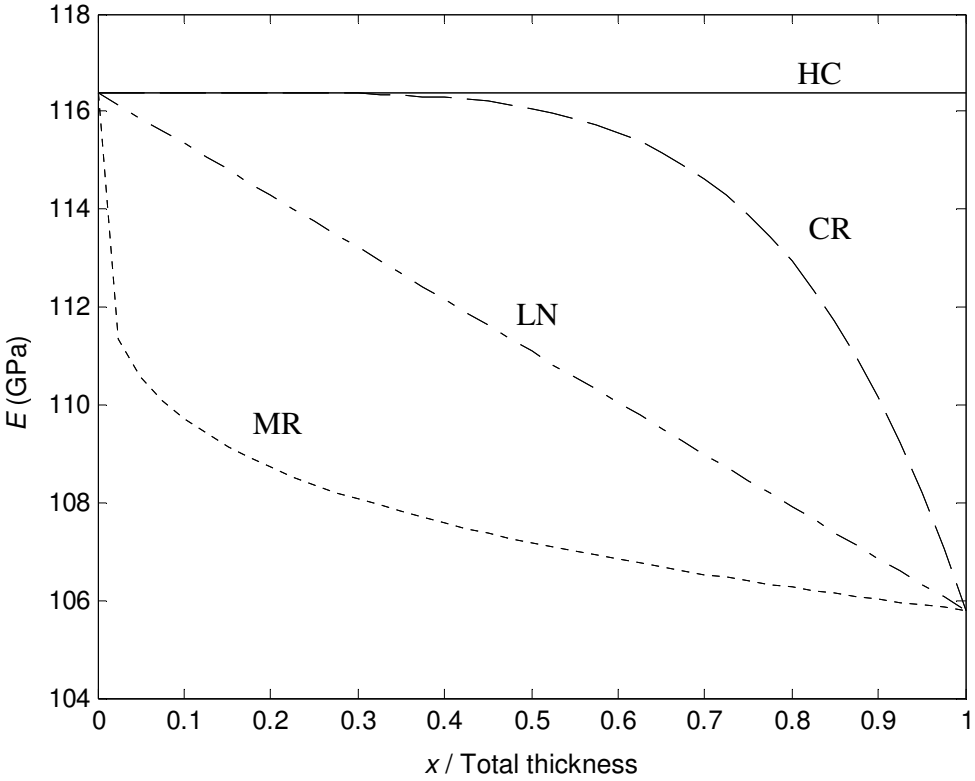

Figure 4.11. Variations of the elastic moduli of different types of FGM

The results for different *a/W* ratios are given in Table 4.3.

Table 4.3. Non-dimensional stress intensity factors *(f)* of bend bar specimen

$$\left(f = \frac{BW^{3/2}}{PS} K_I \right)$$

a/W	*Equation given in ASTM E399*	*HC*	*CR*	*LN*	*MR*
0.45	2.286	2.272	2.322	2.320	2.286
0.55	3.142	3.135	3.209	3.189	3.150
0.65	4.628	4.628	4.739	4.689	4.643
0.75	7.710	7.748	7.925	7.821	7.765
0.85	16.698	16.851	17.158	16.945	16.870
0.95	87.906	83.772	84.411	83.878	83.750

Compact Specimen

The equation for this specimen is

$$K_I = \frac{P}{BW^{1/2}} . f\left(\frac{a}{W}\right) \tag{4.9}$$

where,

$$f\left(\frac{a}{W}\right) = \frac{\left(2+\frac{a}{W}\right)\left(0.886+4.64\frac{a}{W}-13.32\left(\frac{a}{W}\right)^2+14.72\left(\frac{a}{W}\right)^3-5.6\left(\frac{a}{W}\right)^4\right)}{\left(1-\frac{a}{W}\right)^{3/2}} \tag{4.10}$$

The results are given in Table 4.4

Table 4.4. Non-dimensional stress intensity factors *(f)* of compact specimen

$$\left(f = \frac{BW^{1/2}}{P} K_I \right)$$

a/W	*Equation given in ASTM E399*	*HC*	*CR*	*LN*	*MR*
0.45	8.340	8.268	8.398	8.376	8.299
0.55	11.364	11.492	11.711	11.623	11.524
0.65	16.857	16.684	17.033	16.847	16.724
0.75	28.856	29.102	29.690	29.317	29.153
0.85	64.903	65.042	66.058	65.340	65.111
0.95	351.463	349.155	351.502	349.685	349.266

Arc bend Specimen

For the specimen to be used for circular coatings, the equation when $r_1 = 0.5\ r_2$ is given as,

$$K_I = \frac{P}{BW^{1/2}} . f\left(\frac{a}{W}\right) \tag{4.11}$$

where,

$$f\left(\frac{a}{W}\right) = \frac{\left(3.4 + 1.1\frac{a}{W}\right)\left(1 + 0.125\left(1 - \frac{a}{W}\right)^2\right)\left(\frac{a}{W}\right)^{1/2}\left[3.74 - 6.30\frac{a}{W} + 6.32\left(\frac{a}{W}\right)^2 - 2.43\left(\frac{a}{W}\right)^3\right]}{\left(1 - \frac{a}{W}\right)^{3/2}} \tag{4.12}$$

And the results are given in Table 4.5

Table 4.5. Non-dimensional stress intensity factors *(f)* of arc bend specimen

$$\left(f = \frac{BW^{1/2}}{P} K_I \right)$$

a/W	*Equation given in ASTM E399*	*HC*	*CR*	*LN*	*MR*
0.45	13.052	13.056	13.298	13.303	13.126
0.55	17.983	18.069	18.443	18.353	18.144
0.65	26.807	26.992	27.590	27.324	27.066
0.75	45.573	46.165	47.168	46.571	46.242
0.85	100.647	100.663	102.450	101.197	100.756
0.95	467.134	468.541	471.958	469.212	468.550

4.4.1 Evaluation of the Results

All three tables give similar trend in the results. The stress intensity factors of homogeneous ceramic FGM specimen are close to the results of the equation given in ASTM E399. This validates the use of the displacement correlation technique's effectiveness in the determination of stress intensity factors.

The variation of stress intensity values of the specimens is dependent on the $\frac{u_b}{\sqrt{r}}$ ratios which are extrapolated in this study (see eq. (2.4)). The $\sqrt{r}$ expression is constant in all these equations. The difference between the displacements of the nodes determines the SIF results among the specimen types. $\frac{u_{b3}}{\sqrt{R_3}}$ expression is always smaller than $\frac{u_{b2}}{\sqrt{R_2}}$ because the distance to the crack tip of node 3 (R_3) is four time the distance of node 2 (R_2) whereas the difference between the displacements

is not that much (see Figure 2.2). So if $\frac{u_{b3}}{\sqrt{R_3}}$ expression gets smaller or $\frac{u_{b2}}{\sqrt{R_2}}$ expression gets larger, then the calculated SIF value will increase because of the linear extrapolation. The displacements of these nodes are governed with the stiffness of the nodes, therefore the modulus of elasticity values. Ceramic is stiffer than metal and located at the crack opening side. So the displacement of node 3 will be lower than the homogeneous case when compared with node 2. When the displacement of node 3 is even smaller, the difference in $\frac{u_b}{\sqrt{r}}$ will increase and this will give higher SIF value. This means the specimen with maximum variation of material properties among nodes 2 and 3 will give the highest stress intensity factor. CR and LN specimen have the largest SIF values because the change in modulus of elasticity values is largest in these specimens after *a/W* = 0.45 (see Figure 4.11).

4.5 Fatigue Crack Growth Analysis of Test Specimens

4.5.1 Curve Fitting for Fatigue Analysis

The calculation of fatigue crack growth is carried out with the stress intensity factor values for different a/W ratios. Thus curve fitting is applied through the points at which the stress intensity factors are calculated by fitting a polynomial through the points. The curve fitted for ceramic rich compact specimen is shown in Figure 4.12. The curves for other specimens are also created by the same way.

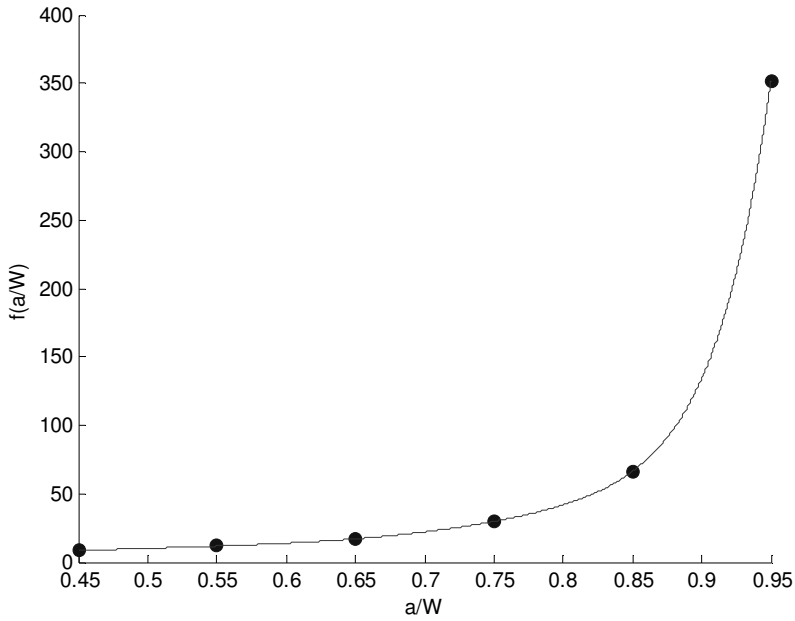

Figure 4.12. Curve fitted through the points of stress intensity factor calculation of ceramic rich compact specimen.

4.5.2 Fatigue Crack Growth Calculation

As discussed before, The Paris-Erdogan formulation is the most widely accepted fatigue crack behavior for region II crack growth analyses. The formulation is,

$$\frac{da}{dN} = C\Delta K^{n} \tag{4.13}$$

In fatigue crack growth study, cyclic mode I loading was given from 0 to some load P. So ΔK will be the stress intensity factor found with the application of P. The critical point here is the determination of the parameters C and n in the structure. The values of these parameters differ too much in metals and ceramics. These material properties are also assumed to be varied by the variation function of material properties in the FGM specimens. In the calculation of crack growth, the

position of the crack tip determines the C and n parameters in the cycle. In this study, SIF values being equal to K_{IC} values are the failure criteria. Thus, the analyses of the specimens are carried out up to K_{IC} values are reached to determine the life of the specimens under the given load. Because of K_{IC} being a material property, it is also assumed that it is varied with the variation function given for the material properties of specimens. The equations are

$$K_{IC}(y) = K_{ICc} + (K_{ICm} - K_{ICc})(y/W)^p \quad \text{for bend bar specimen} \quad (4.14)$$

$$K_{IC}(x) = K_{ICc} + (K_{ICm} - K_{ICc})(x/1.25W)^p \quad \text{for compact specimen} \quad (4.15)$$

$$K_{IC}(r) = K_{ICc} + (K_{ICm} - K_{ICc})[(r - r_1)/(r_2 - r_1)]^p \quad \text{for arc bend specimen} \quad (4.16)$$

The C and n values as well as the critical stress intensity factors used in this study are given in Table 4.6. The values of C and n parameters given in the table are valid when the unit of ΔK is $MPa.m^{1/2}$ and *da/dN* is *m/cycle*.

Table 4.6. Paris – Erdoğan Law constants and K_{IC} values used in the study [34,36,43]

	C	n	K_{IC} $(MPa.m^{1/2})$
ZrO_2	2.7×10^{-16}	19	5
Ti-6Al-4V	5.2×10^{-12}	3.17	75

In the analysis of fatigue crack growth, the parameters are changing according to the coordinates of the crack tip, so (4.13) is used as,

$$\frac{\Delta a}{\Delta N} = C(x)(\Delta K_I(x))^{n(x)} \quad (4.17)$$

Here x direction is the direction of crack growth. Δa gives the crack growth in ΔN cycles. At each cycle, ΔK value is calculated using the new crack length (*a)* and the

curve fitted for different *a/W* ratios. *C(x)* and *n(x)* values are determined according to the position of the crack tip. The crack growth Δa is calculated by (4.17) using $\Delta N = 1$ and $x=a$. The dimensions of the specimens used in the analyses are given in Table 4.7.

Table 4.7. Dimensions of test specimens

Specimen width (W-mm)	*Specimen thickness (B-mm)*	*Arc bend specimen inner radius (r_1-mm)*	*Arc bend specimen outer radius (r_2-mm)*
40	20	40	80

4.6 Fatigue Crack Growth Results

Analyses are carried out for different initial crack lengths and loading conditions. The results are given in Table 4.8 through Table 4.13. The results are plotted with respect to number of cycles versus the crack length to compare the crack growth among FGM types in Figure 4.13 through Figure 4.18.

Table 4.8. Crack lengths for the bend bar specimen subjected to 1100 N cyclic loading, initial crack length = 18 mm

Specimen type	*HC*	*CR*	*LN*	*MR*
Crack length after 100 cycles (mm)	18.0009649	18.6735912	18.0158236	18.0000704
Last crack length calculated before failure (mm)	-	25.4503641	37.3609707	-
Last SIF calculated before failure(MPa.m$^{1/2}$)	-	4.9035	67.6381	-
Critical SIF before failure (MPa.m$^{1/2}$)	5	12.2991	70.3817	-
Crack length after 20000 cycles (mm)	18.2338110	-	-	18.0142523
Number of cycles to failure	>20000	150	12270	>20000

Table 4.9. Crack lengths for the bend bar specimen subjected to 190 N cyclic loading, initial crack length = 34 mm

Specimen type	*HC*	*CR*	*LN*	*MR*
Crack length after 100 cycles (mm)	34.1574933	34.5542834	34.0002862	34.0000361
Last crack length calculated before failure (mm)	35.0749763	37.6729175	-	-
Last SIF calculated before failure(MPa.m$^{1/2}$)	4.4825	13.6656	-	-
Critical SIF before failure (MPa.m$^{1/2}$)	5	56.8734	-	-
Crack length after 20000 cycles (mm)	-	-	34.0597272	34.0073125
Number of cycles to failure	172	146	>20000	>20000

Table 4.10. Crack lengths for the compact specimen subjected to 1200 N cyclic loading, initial crack length = 18 mm

Specimen type	*HC*	*CR*	*LN*	*MR*
Crack length after 100 cycles (mm)	18.0008388	19.7247767	18.2199716	18.0000401
Last crack length calculated before failure (mm)	-	23.7457721	-	-
Last SIF calculated before failure(MPa.m$^{1/2}$)	-	4.0494	-	-
Critical SIF before failure (MPa.m$^{1/2}$)	5	14.8027	-	-
Crack length after 20000 cycles (mm)	18.2066425	-	19.3326969	18.0081228
Number of cycles to failure	>20000	110	>20000	>20000

Table 4.11. Crack lengths for the compact specimen subjected to 200 N cyclic loading, initial crack length = 34 mm

Specimen type	*HC*	*CR*	*LN*	*MR*
Crack length after 100 cycles (mm)	34.2813659	34.1001051	34.0188682	34.0000339
Last crack length calculated before failure (mm)	35.2543845	37.9967101	-	-
Last SIF calculated before failure(MPa.m$^{1/2}$)	4.9179	17.5450	-	-
Critical SIF before failure (MPa.m$^{1/2}$)	5	62.0565	-	-
Crack length after 20000 cycles (mm)	-	-	34.0377520	34.0068735
Number of cycles to failure	126	560	>20000	>20000

Table 4.12. Crack lengths for the arc bend specimen subjected to 750 N cyclic loading, initial crack length = 18 mm

Specimen type	*HC*	*CR*	*LN*	*MR*
Crack length after 100 cycles (mm)	18.0006529	18.3339625	18.0120488	18.0000625
Last crack length calculated before failure (mm)	-	25.4583185	37.3432464	-
Last SIF calculated before failure(MPa.m$^{1/2}$)	-	4.8592	64.6784	-
Critical SIF before failure (MPa.m$^{1/2}$)	5	12.3105	70.3507	-
Crack length after 20000 cycles (mm)	18.1482028	-	-	18.0126609
Number of cycles to failure	>20000	232	15392	>20000

Table 4.13. Crack lengths for the arc bend specimen subjected to 130 N cyclic loading, initial crack length = 34 mm

Specimen type	*HC*	*CR*	*LN*	*MR*
Crack length after 100 cycles (mm)	34.3435890	34.9132669	34.0003221	34.0000390
Last crack length calculated before failure (mm)	35.0462969	37.7502880	-	-
Last SIF calculated before failure(MPa.m$^{1/2}$)	4.477	13.6269	-	-
Critical SIF before failure (MPa.m$^{1/2}$)	5	57.4082	-	-
Crack length after 20000 cycles (mm)	-	-	34.0673721	34.0079117
Number of cycles to failure	119	123	>20000	>20000

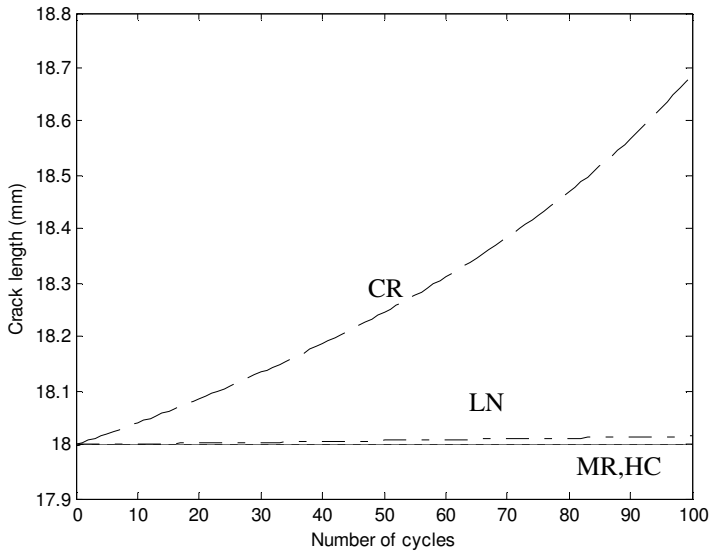

Figure 4.13. Number of cycles versus crack length for bend bar specimen with initial crack length 18 mm and 1100 N cyclic load

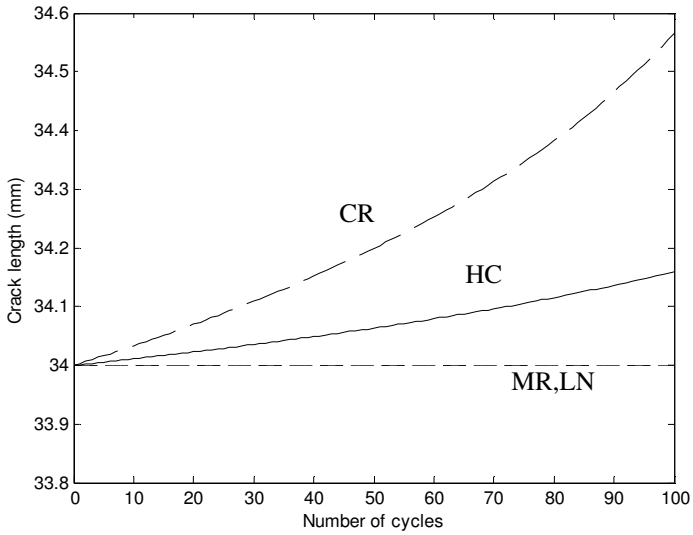

Figure 4.14. Number of cycles versus crack length for bend bar specimen with initial crack length 34 mm and 190 N cyclic load

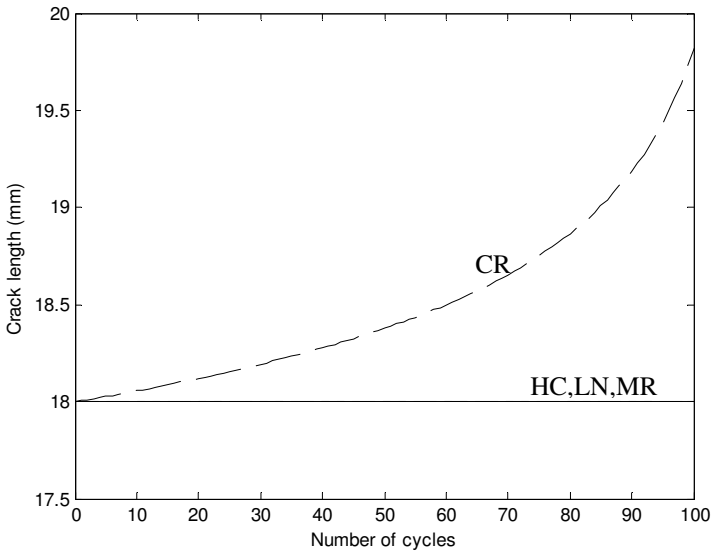

Figure 4.15. Number of cycles versus crack length for compact specimen with initial crack length 18 mm and 1200 N cyclic load

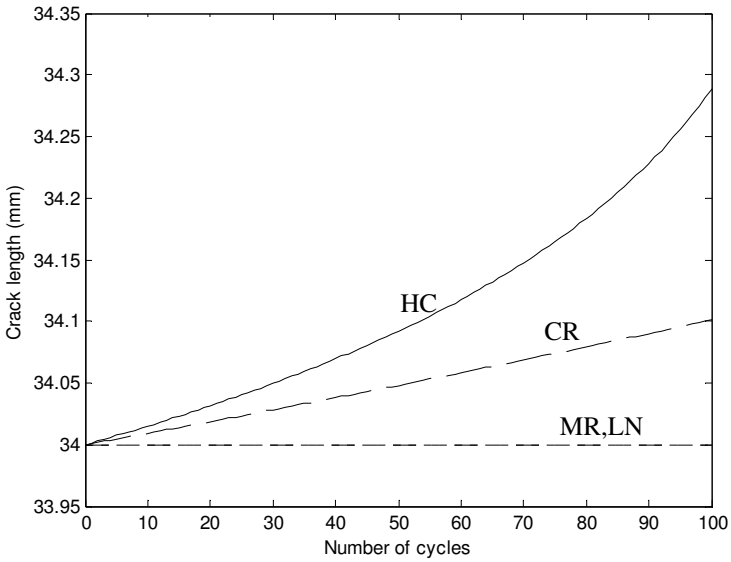

Figure 4.16. Number of cycles versus crack length for compact specimen with initial crack length 34 mm and 200 N cyclic load

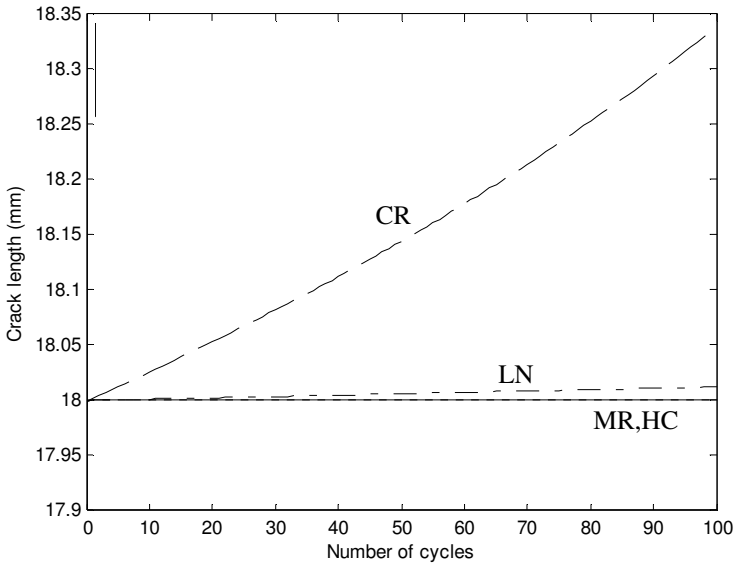

Figure 4.17. Number of cycles versus crack length for arc bend specimen with initial crack length 18 mm and 750 N cyclic load

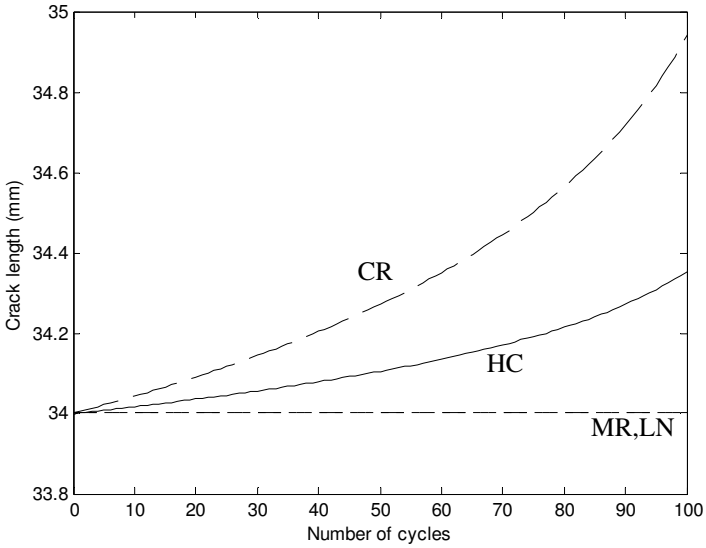

Figure 4.18. Number of cycles versus crack length for arc bend specimen with initial crack length 34 mm and 130 N cyclic load

4.7 Discussion of the Results

Bend bar Specimen

According to the results, the crack growth rate of CR specimen is the largest for 100 cycles and 18 mm crack length when compared with HC, LN and MR specimens. Also fewer number of cycles are required for the failure of CR specimen. The *C* parameter of metal is higher whereas the *n* parameter is higher for ceramic. For CR specimen when crack length is small the change in *C* parameter is dominant against the *n* parameter so crack growth rate is higher for CR specimen when compared with HC specimen. For LN and MR specimens change in the *n* parameter is too much with the increased metal content and this causes very high fatigue life.

The number of cycles required for the failure of CR specimen is very low when compared to other two specimens. The difference between the last calculated stress intensity factor and critical stress intensity factor is too much because after 150th cycle, rapid crack growth is observed so the exact point where the critical SIF value reached could not be determined.

When crack length is large, the initial crack tip is very close to the homogeneous metal side for the CR specimen. This results in *n* parameter being lower for CR specimen and the crack growth rate of HC & CR specimens becomes closer.

Compact Specimen

Similar results are obtained for the compact specimen with a small difference. When the crack length is 34 mm, crack growth value of HC specimen for 100 cycles is more than CR specimen. This result comes from the formulation of variation of material properties for compact specimen. At this crack length, the metal content at the crack tip is higher when compared with the bend bar specimen.

This makes the crack growth rate of CR specimen lower than HC specimen because of its increased metal content.

Arc Bend Specimen

The results resemble the results of bend bar specimen. Thus same discussions apply for this specimen also. The variation formulation of material properties being the same causes this situation.

CHAPTER 5

FATIGUE CRACK GROWTH ANALYSIS IN THREE DIMENSIONS

5.1 Introduction

In the previous chapter, the crack growth is analyzed with the plane strain assumption. But for real applications, cracks generally do not exist along the specimen but occur as a void in the material.

The cracks determined by ultrasonic applications are generally assumed to be in elliptical shape so in this study elliptical crack growth in an FGM medium will be analyzed. The crack geometry is shown in Figure 5.1. The stress intensity factors should be determined initially to determine the crack growth behavior.

For the case of an embedded flat elliptical crack loaded in tension, Irwin [44] derived an expression for the determination of stress intensity factors along the crack profile.

$$K_I = \frac{\sigma\sqrt{\pi a}}{\Phi}\left[\left(\frac{a}{c}\right)^2 \cos^2\phi + \sin^2\phi\right]^{1/4} \tag{5.1}$$

where,

$$\Phi = \int_0^{\pi/2}\left[1-\left(\frac{c^2-a^2}{c^2}\right)\sin^2\phi\right]^{\frac{1}{2}} d\phi \tag{5.2}$$

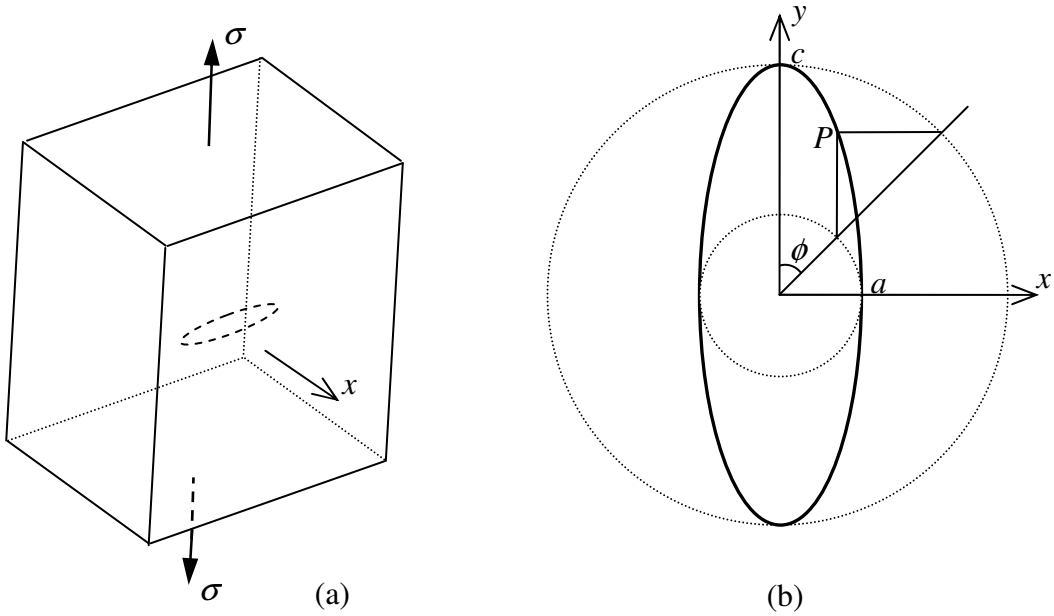

Figure 5.1. (a) Elliptical crack in an infinite medium, (b) The parametric Ø angle to determine the location of point P on the ellipse

In some of the studies in the literature fatigue crack growth model of elliptical cracks is based on the assumption that the elliptical crack form never changes [45]. Thus the new crack form is calculated by only evaluating the new major axis crack length (c) and minor axis crack length (a). By this way new stress intensity factors can again be calculated by equation (5.1) and new crack form can be obtained.

In general it is known that this assumption gives accurate results for homogeneous materials. But for FGMs, this assumption cannot be used. The different fatigue crack growth behavior of ceramic and metal in the structure alters the crack growth profile. So the only way to calculate the crack growth in these structures is the use of numerical techniques such as finite element method.

In this study, a procedure for the 3-D fatigue crack growth model of elliptical cracks that can be used for FGM materials is developed by using the finite element technique. Similar to the 2-D case, stress intensity factors are first calculated by

using the displacement correlation technique. Paris – Erdoğan Law is used to calculate the crack growth at certain points on the crack profile. All the procedures are carried out by developing APDL codes. The procedure for the modeling of the elliptical crack and the determination of stress intensity factors are adapted from [15]. By the help of the code, crack profile for a certain number of cycles under a given load can be calculated.

5.2 Crack Growth Analysis in Homogeneous Medium

At first, stress intensity factors are calculated for an elliptical crack in a homogeneous medium to validate the model by comparing the results to the results of Irwin [44]. The crack growth profiles for certain loads are calculated and compared with the assumption that elliptical crack form never changes.

5.2.1 Modeling of Elliptical Crack Region

As the crack in the volume is symmetrical in x and y directions, one forth of the crack is modeled. The APDL code starts with asking the user, minor (a) and major axes (c) lengths of the elliptical crack. According to the crack form, 17 points are drawn with the same angle $\emptyset$ increment and a segmented spline is passed through these points (Figure 5.2). One half of these spline segments (the left-hand side) is created to make the line 8 be perpendicular to point 9 and will not be used in the analyses. Otherwise it would create problems in applying the symmetry. The analysis will be carried out for the first 9 keypoints and these are the points to be used for calculation of stress intensity factors for fatigue crack growth.

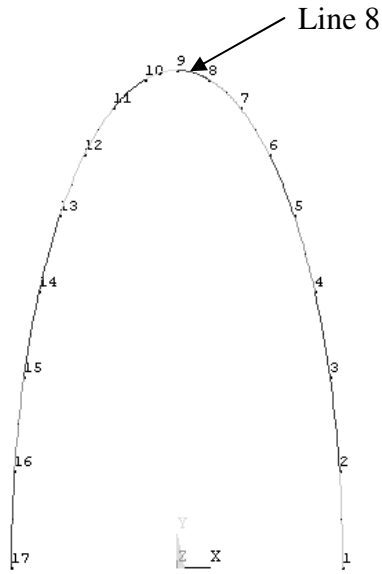

Figure 5.2. Segmented spline passed through 17 points representing the crack front

An area is drawn near the minor axis and concentrated mesh is applied at keypoint 1. The element type used is Mesh200 element. This element does not contribute directly to the solution but used for multi-step meshing operations, such as extrusion, that require a lower dimensionality mesh be used for the creation of a higher dimensionality mesh [26]. The meshed area is dragged along the segments of lines repeatedly and meshed volumes are generated at the crack growth calculation points (Figure 5.3). The generated volumes' element type is Solid 95. Figure 5.4 shows one of the volumes created with the concentrated mesh at the crack growth calculation points.

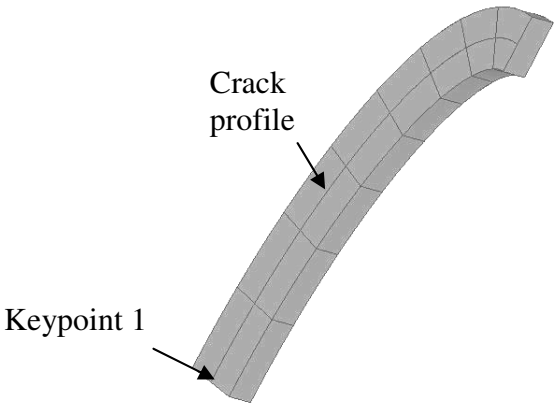

Figure 5.3. Meshed volumes generated by dragging the meshed areas along the spline segments.

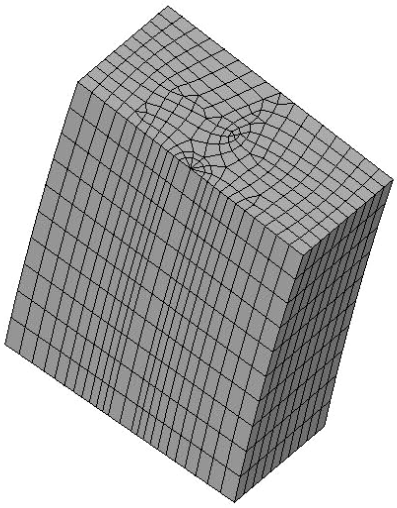

Figure 5.4. Mesh structure of one of the volumes

5.2.2 Modeling of Infinite Medium

The crack is assumed to be located in an infinite medium. Thus the medium is modeled as a huge cube whose sides are very large compared to elliptic crack dimensions to eliminate the free surface effects. First a small prism is created by generating volumes inside and outside the volumes generated around the crack region (Figure 5.5). The procedure is straightforward; creating points, straight lines from the points, areas from the lines and volumes from the areas. Figure 5.6 shows the whole model generated by the same way.

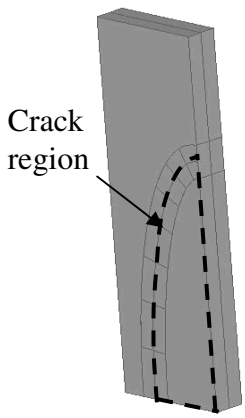

Figure 5.5. Volumes around crack region

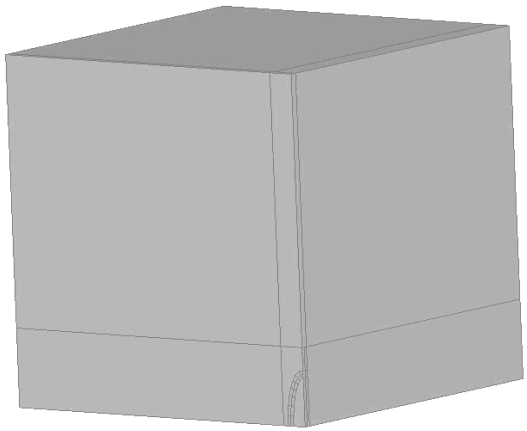

Figure 5.6. The whole model

5.2.3 Meshing and Boundary Conditions

The volumes at the crack region are already meshed. The other volumes are meshed with fixed element size (ESIZE command). The mesh structure at these regions does not contribute too much to the analyses results but for the analyses to run without errors, less deformed elements should be generated. The prismatic volumes far away from the crack are meshed with Solid95 brick elements whereas the arbitrary volumes near the crack region are meshed with Solid92 tetrahedral elements (Figure 5.7). They both have quadratic shape functions with their nodes having three degrees of freedom (Figure 5.8).

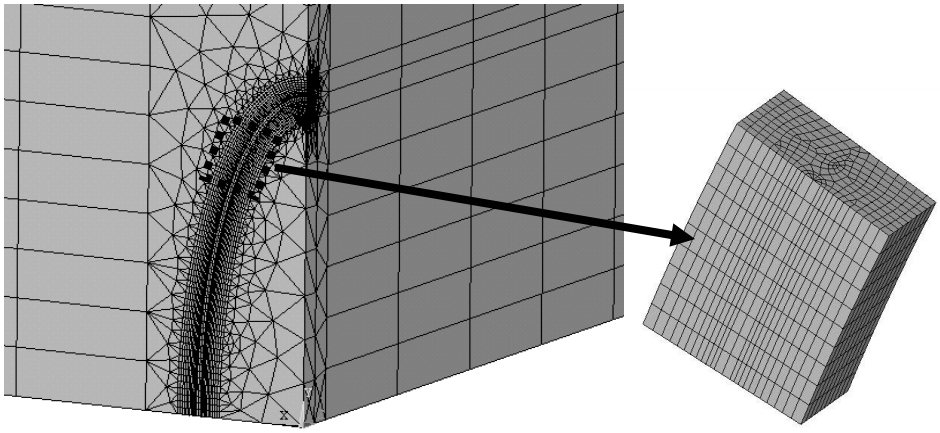

Figure 5.7. The mesh structure in the model

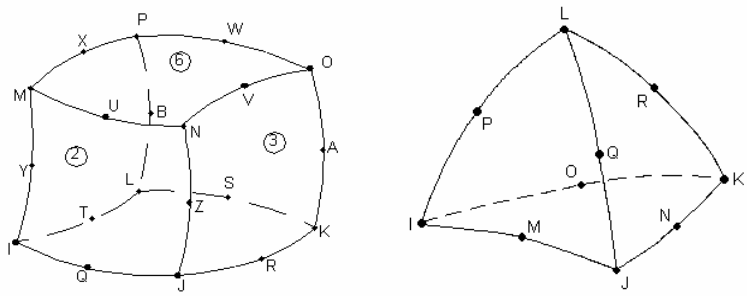

(a) (b)

Figure 5.8. (a) Solid95 (b) Solid92 elements [26]

As this is the one forth model of the whole structure, symmetrical boundary condition is given to the sides. Care should be taken in the application of symmetrical boundary conditions; yet it should not be applied at the crack region. Applied loading is uniform tension σ and perpendicular to the crack plane as shown in Figure 5.1. The boundary conditions are shown in Figure 5.9. After the assignment of mechanical material properties, the analysis is ready to be run.

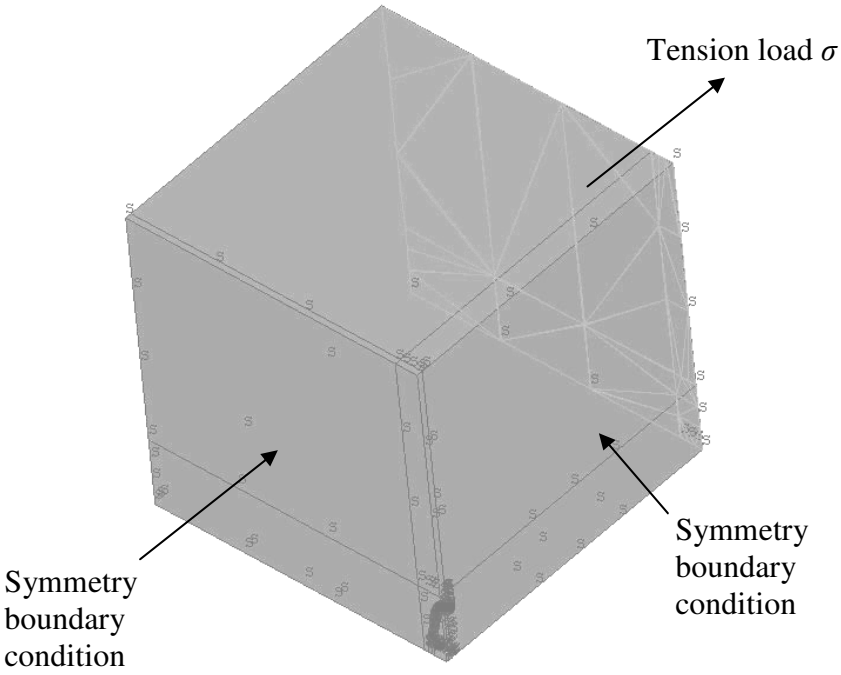

Figure 5.9. Boundary Conditions

5.2.4 Postprocessing and Stress Intensity Factor Calculation

After the solution is done, Mode I stress intensity factors are calculated at the 9 keypoints by using the displacement correlation technique. For the calculations a new coordinate system is defined at each keypoint perpendicular to crack front. Figure 5.10 shows the region close to one of the keypoints. The figure on the right is the triangular singular element towards the nodes of which will be used in the calculation of SIF using displacement correlation technique.

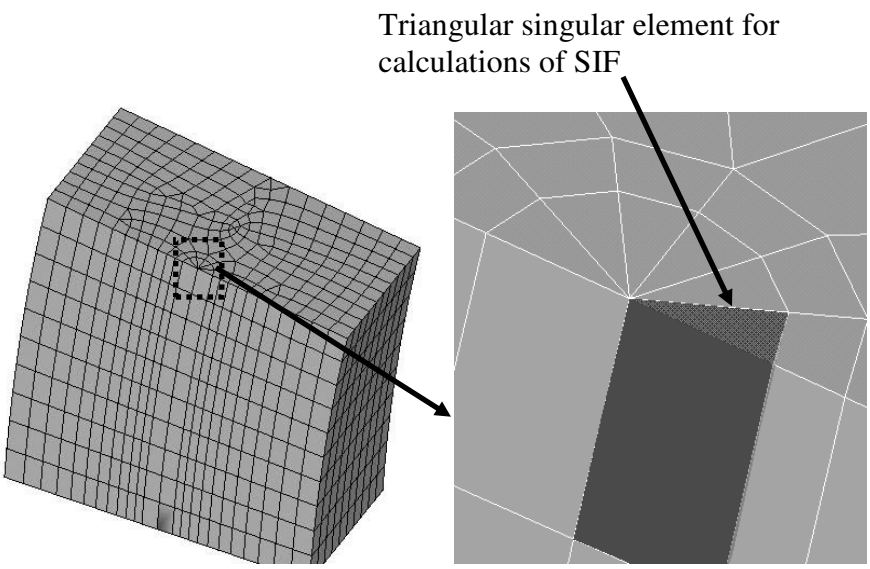

Figure 5.10. The mesh structure near one of the 9 keypoints

5.2.5 Stress Intensity Factors for Elliptical Crack

To validate the model, the stress intensity factors along the 9 keypoints are determined and compared to the results of Irwin [44]. The elliptical crack shape is created with major and minor axis lengths of 1.5 cm and 0.5 cm respectively. Non-dimensional stress intensity factor (*f*) is defined as;

$$f = \frac{K_I}{\sigma\sqrt{\pi a}} \tag{5.3}$$

Comparison of the stress intensity factors are given in Table 5.1. The positions of 9 keypoints are determined by parametric angle *Ø*. It can be said that the results of the present study are very close to the results of Irwin [44]. The stress intensity factor values are getting larger towards the minor axis so crack development is expected to be more in the minor axis direction.

Table 5.1. Non-dimensional stress intensity factor comparison for a = 0.5 cm and c = 1.5 cm

2Ø/π	***Keypoint Number***	***Irwin [44]***	***Present Study***	***% Difference***
0 (major axis)	9	0.5184	0.5195	0.21
0.125	8	0.5540	0.5551	0.20
0.25	7	0.6293	0.6304	0.17
0.375	6	0.7075	0.7085	0.14
0.5	5	0.7752	0.7759	0.09
0.625	4	0.8287	0.8290	0.04
0.75	3	0.8671	0.8668	0.03
0.875	2	0.8902	0.8892	0.11
1 (minor axis)	1	0.8979	0.8969	0.11

5.2.6 Fatigue Crack Growth Calculations

The crack growth modeling method is adapted from the technique described by Joseph and Erdogan [46]. Here, there are 9 keypoints around the ellipse that the stress intensity factors are calculated. The crack growth rate of these points can be expressed as,

$$\frac{\Delta a_i}{\Delta N} = C\Delta K_i^{\,n} \tag{5.4}$$

where the subscript i shows the keypoint number. To start the computations, first a sufficiently small Δa_1 which is the crack growth of keypoint 1 is selected. The number of cycles to reach that crack length can be calculated from equation (5.4) as,

$$\Delta N = \frac{\Delta a_1}{C\Delta K_1^{\ n}} \tag{5.5}$$

The crack growth at the other 8 points can be found from

$$\Delta a_i = \frac{C\Delta K_i^{\ n}}{C\Delta K_1^{\ n}} \Delta a_1 \tag{5.6}$$

The calculated crack growth values are added to the location of the keypoints by defining the coordinate system at those keypoints perpendicular to the crack front. These new coordinates are stored in a file and ready to be read for the modeling of next group of cycles. The calculations are carried out for Ti-6Al-4V with 100 MPa tension load. Material properties are given in Chapter 4.

Next, the database is cleared and the new points of calculations are read from the stored file. The keypoints are generated and a spline is passed through them creating the new crack profile. The rest of the calculations are the same. Continuing these calculations gives the subsequent crack growth profiles for certain number of cycles.

5.2.7 Fatigue Crack Growth Analysis Results

The crack front profiles obtained after 4 consecutive analyses are given in Figure 5.11. In the analyses constant crack growth increment in minor axis direction is given as 0.2 cm. The profiles that would be obtained with the assumption that elliptical crack form never changes is also shown in this figure.

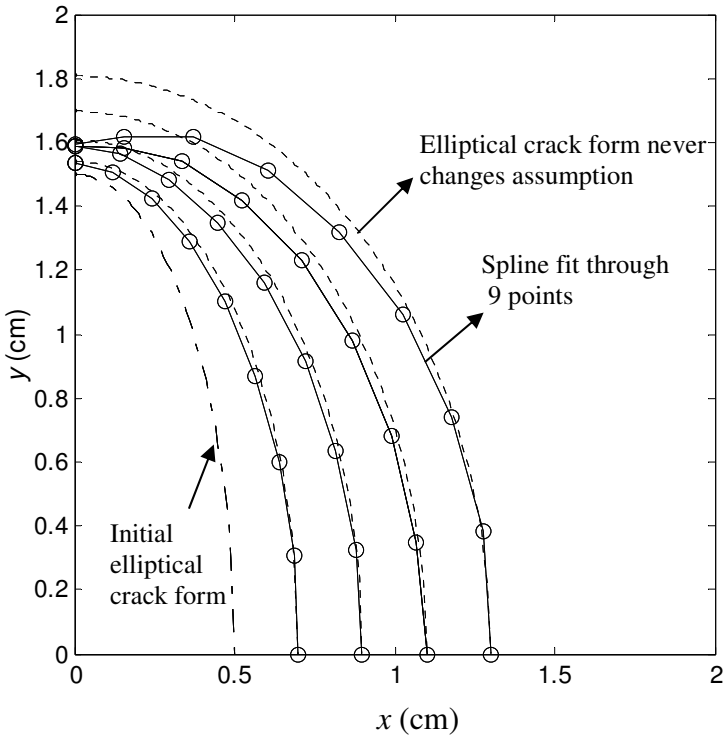

Figure 5.11. Fatigue crack growth analysis results with the quarter model for homogeneous Ti-6Al-4V

As it is seen in Figure 5.11, the crack profiles calculated by the present study is similar to the crack profiles obtained by the assumption of elliptical crack form never changes upto first two analyses. But in third and fourth analyses, it was observed that the crack growth at the keypoints close to y-axis is very small and leaves the path of the profiles obtained by the elliptical crack form never changes assumption. It was understood that this problem is occurred because of the symmetry boundary condition given on the areas along y-axis. After dragging the meshed areas along the segmented splines (see Figure 5.3), the last obtained area should be perpendicular to y-axis to define the symmetry at this area. In the first and second analyses, there were no problems about this. But in third and the fourth analyses, this area leaves the direction of y axis. Figure 5.12 explains the situation. The x coordinate of keypoint 59 and keypoint 57 should be equal to zero. But

because of the error in the dragging operation, their x coordinates are 0.52 and -0.32 respectively. This means that the side of the area is not parallel to y-axis.

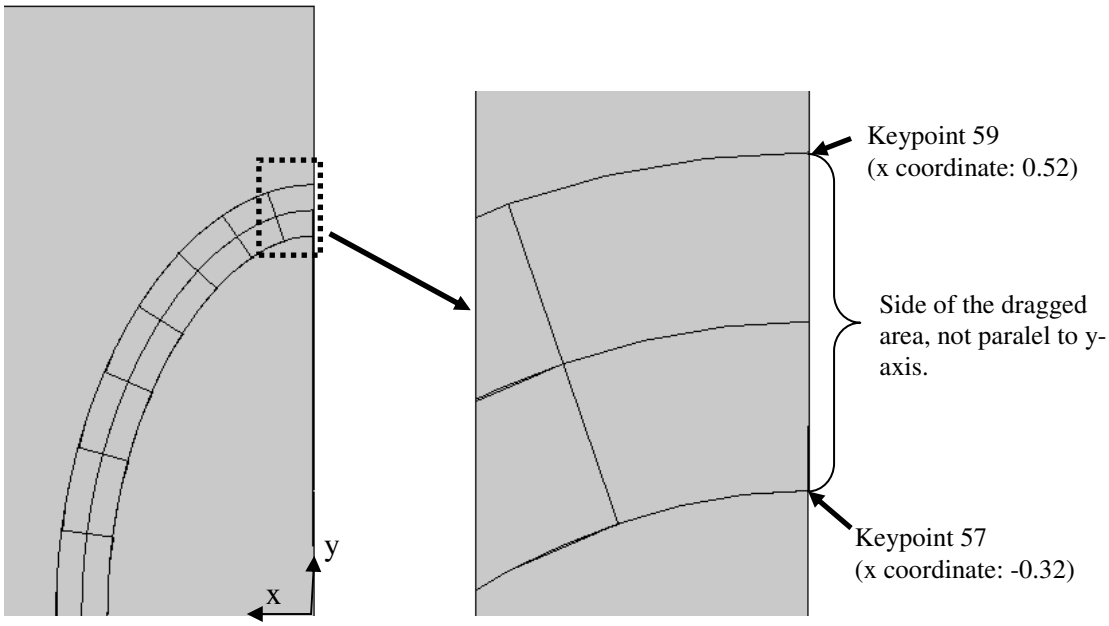

Figure 5.12. Representation of error occurred after third analysis

Thus, in order to solve this problem, instead of quarter, model, one half of the model is generated with the same procedure. The model is shown in Figure 5.13. The number of keypoints for the calculation of crack growth is increased to 17. The results are obtained with this half model again and shown in Figure 5.14. It was seen that, the problem is solved and the results obtained are very similar to the assumption of elliptical crack form never changes in third and fourth analyses also.

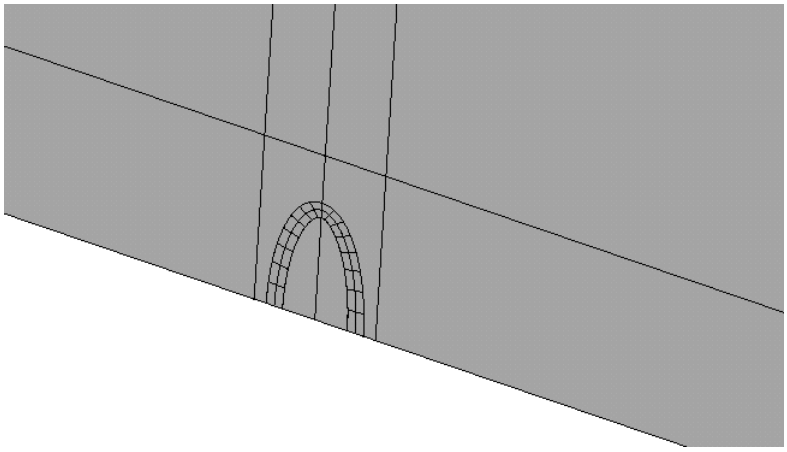

Figure 5.13. The half finite element model

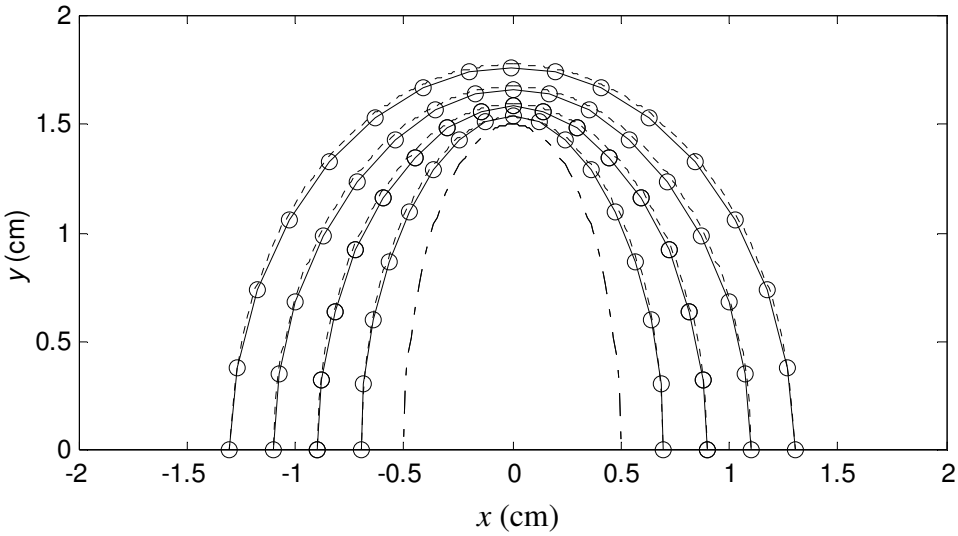

Figure 5.14 Fatigue crack growth analysis results with the half model for homogeneous Ti-6Al-4V

The number of cycles to reach the crack profiles in Figure 5.14 is given in Table 5.2. It is observed that fewer cycles are required to reach the next crack profile. It is expected as well because as the crack develops, the calculated stress intensity factor values increases, leading for the need of fewer cycles for the crack growth.

Table 5.2. Cycle numbers for reaching the crack profiles

Profile	Number of cycles (N)
1	178,943
2	128,383
3	102,057
4	85,486

5.3 Elliptical Fatigue Crack Growth in FGM Structures

In this section, two different crack configurations are considered. In one of the cases, material property variation is along the minor axis, in the other case, variation is along the major axis.

5.3.1 3D Finite Element Modeling of FGM Structure with an Elliptical Crack Inside

The case study of elliptical crack in FGM structure is shown in Figure 5.15. The crack is located on the symmetry plane (z=0) and closer to the 100% metal side. The total thickness (H) is given as 15 cm.

In this model the material properties are assumed to be varying exponentially. If the modulus of elasticity is considered, the variation is given as,

$$E(x) = E_c \exp\left(\beta\left(2H/3 - x\right)\right) \tag{5.7}$$

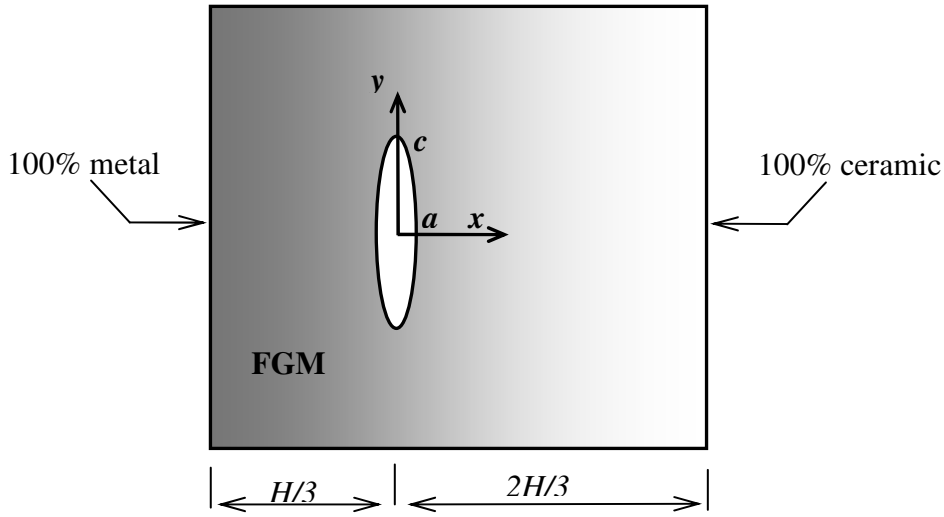

(a)

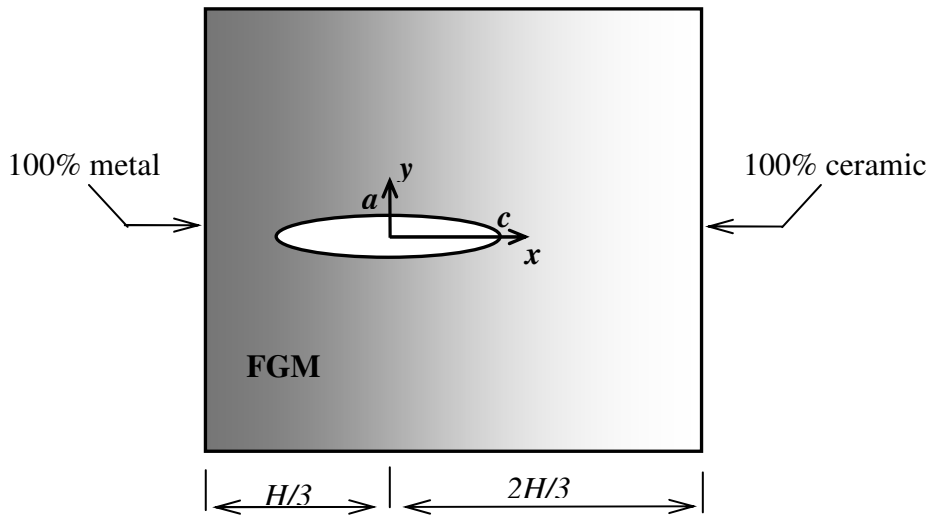

(b)

Figure 5.15. Elliptical crack in an FGM medium; (a) variation along minor axis, (b) variation along major axis

where,

$$\beta = \frac{1}{H} \ln\left(\frac{E_m}{E_c}\right) \tag{5.8}$$

The modulus of elasticity of 100% metal and 100% ceramic sides can be expressed as;

$$E_m = E(-H/3), \qquad E_c = E(2H/3) \tag{5.9}$$

Exactly, same kind of variations is used for the other material parameters. The variation is again given to the centroidal coordinates of the elements like the procedure explained in chapters 2 and 4.

The part of the finite element model generated for the analysis for the variation along minor axis is depicted in Figure 5.16. One half of the model is generated again and the number of keypoints of calculations is again 17.

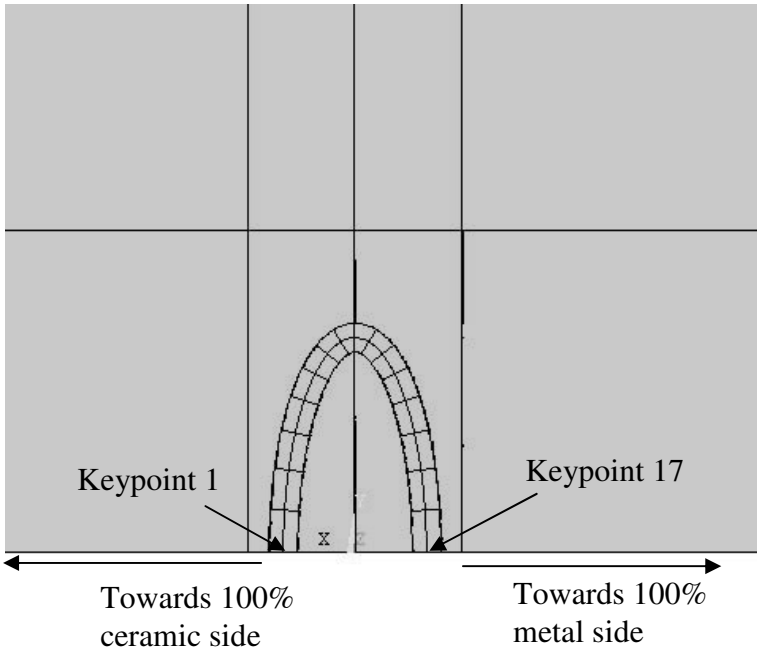

Figure 5.16. FGM modelling with elliptical crack inside (variation along minor axis)

The ceramic and metal components used in the chapter are again Zirconia and Ti-6Al-4V respectively. Their properties are given in Chapter 3. Cyclic loading of 100 MPa is applied with the same initial crack major and minor axis lengths 1.5 and 0.5 cm respectively as given in the homogeneous structure. The critical stress intensity factor (K_{IC}) is also defined according to variation function given in equations (5.7) and (5.8). After each analysis safety factors are determined by dividing the K_{IC} value at the 17 points to SIF value of each keypoint. The constant crack growth value of 0.2 cm is given after each run in the analysis of variation along minor axis direction case.

For the analysis of functionally graded material, whose variation is along the major axis direction, same procedure is applied with exchanging the crack major and minor axes (Figure 5.17). The crack growth given to the major axis is adjusted

according to number of cycles to reach each profile will be the same like the variation along minor axis case.

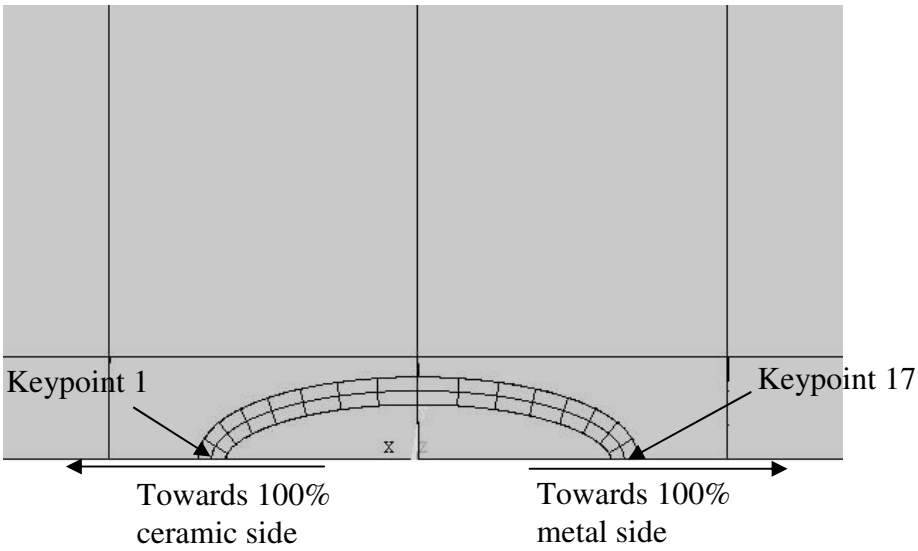

Figure 5.17. FGM modelling with elliptical crack inside (variation along major axis)

5.3.2 Results Computed for Variation in Minor Axis Direction

The profiles reached after 4 consecutive analyses are shown in Figure 5.18. Calculated stress intensity factors are given in Table 5.3. The K_{IC} values calculated at each keypoint are divided to the SIF values to determine the safety factor after the next run for each crack form. The results are shown in Table 5.4. The number of cycles to reach each crack profile is given in Table 5.5.

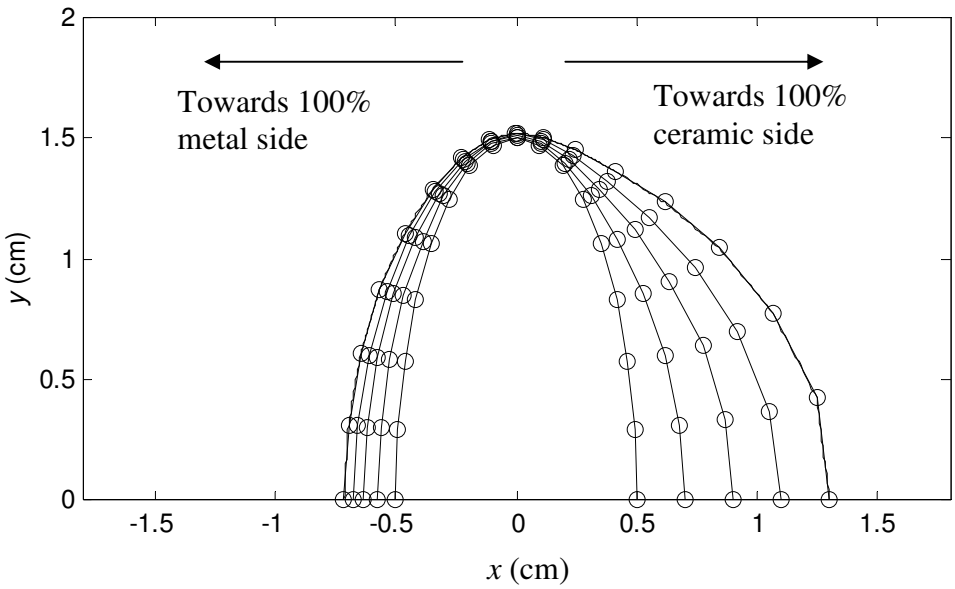

Figure 5.18. Elliptical crack forms obtained (variation along minor axis)

Table 5.3. Calculated stress intensity factors (Mpa.m$^{1/2}$)

Keypoint number	***Original crack profile***	***Crack profile 1***	***Crack profile 2***	***Crack profile 3***	***Crack profile 4***
1	11.261	11.809	12.273	12.418	13.125
2	11.164	11.780	12.176	12.620	12.620
3	10.882	11.607	12.109	12.506	13.038
4	10.409	11.250	11.923	12.398	12.918
5	9.725	10.688	11.473	12.165	12.709
6	8.865	9.809	10.772	11.547	12.339
7	7.861	8.743	9.667	10.608	11.498
8	6.924	7.681	8.498	9.354	10.332
9	6.491	7.165	7.879	8.612	9.444
10	6.929	7.600	8.281	8.948	9.659
11	7.862	8.565	9.247	9.865	10.483
12	8.851	9.584	10.246	10.810	11.366
13	9.720	10.463	11.102	11.644	12.154
14	10.392	11.159	11.795	12.308	12.804
15	10.866	11.659	12.290	12.799	13.276
16	11.148	11.962	12.608	13.087	13.574
17	11.244	12.067	12.699	13.192	13.665

Table 5.4. Safety factors for each profile

Keypoint number	***Original crack profile***	***Crack profile 1***	***Crack profile 2***	***Crack profile 3***	***Crack profile 4***
1	2.467	2.270	2.106	2.008	**1.832**
2	2.493	2.284	2.136	1.995	1.924
3	2.571	2.344	2.184	2.060	1.924
4	2.711	2.458	2.273	2.145	2.023
5	2.934	2.637	2.426	2.262	2.141
6	3.263	2.931	2.652	2.459	2.287
7	3.737	3.352	3.024	2.749	2.529
8	4.315	3.888	3.511	3.187	2.884
9	4.685	4.245	3.860	3.531	3.220
10	4.467	4.075	3.742	3.465	3.212
11	4.004	3.682	3.416	3.207	3.022
12	3.613	3.349	3.143	2.987	2.849
13	3.335	3.118	2.954	2.829	2.721
14	3.155	2.964	2.825	2.723	2.631
15	3.042	2.867	2.745	2.654	2.574
16	2.981	2.813	2.696	2.618	2.541
17	2.960	2.795	2.684	2.605	2.532

Table 5.5. Number of cycles to reach each crack profile

Crack profile	***Number of cycles***
1	5,359
2	3,170
3	1,943
4	1,391

5.3.3 Results Computed for Variation in Major Axis Direction

Similarly 4 consecutive analyses are run for this case also. The crack forms obtained are shown in Figure 5.19. The calculated stress intensity factor values are given in Table 5.6 and the safety factors are given in Table 5.7. The cycle numbers to reach these profiles are given in Table 5.8.

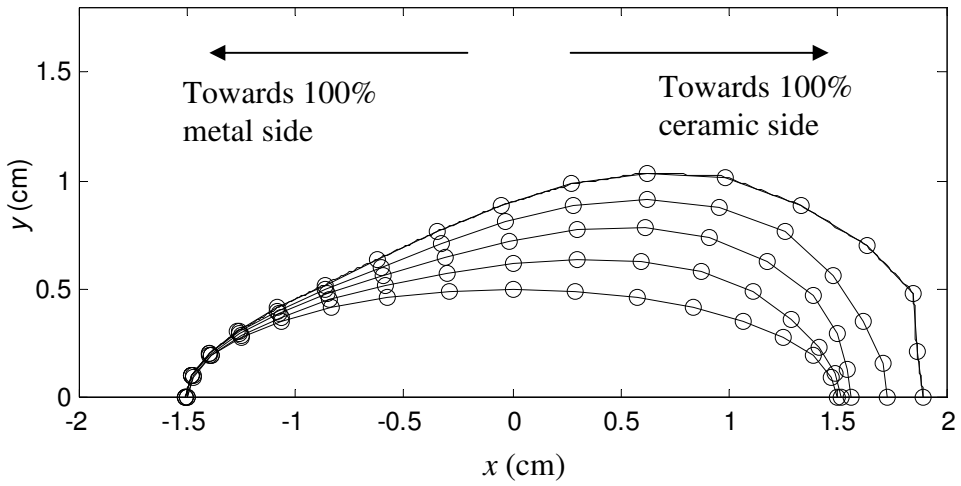

Figure 5.19. Elliptical crack forms obtained (variation along major axis)

Table 5.6. Calculated stress intensity factors (Mpa.m$^{1/2}$)

Keypoint number	***Original crack profile***	***Crack profile 1***	***Crack profile 2***	***Crack profile 3***	***Crack profile 4***
1	6.493	8.127	10.569	10.798	11.611
2	6.930	8.607	10.503	10.806	13.718
3	7.869	9.444	10.253	11.760	10.192
4	8.860	10.064	10.522	11.683	12.340
5	9.720	10.511	11.214	11.554	13.044
6	10.390	11.023	11.678	12.267	12.752
7	10.866	11.562	12.117	12.759	13.427
8	11.153	11.986	12.558	13.133	13.806
9	11.247	12.181	12.850	13.427	14.039
10	11.152	12.068	12.858	13.475	14.098
11	10.865	11.692	12.478	13.156	13.798
12	10.379	11.107	11.796	12.426	13.047
13	9.712	10.314	10.892	11.434	11.965
14	8.850	9.347	9.822	10.264	10.700
15	7.858	8.278	8.669	9.037	9.387
16	6.918	7.278	7.607	7.919	8.221
17	6.474	6.819	7.123	7.408	7.683

Table 5.7. Safety Factors for each profile

Keypoint number	***Original crack profile***	***Crack profile 1***	***Crack profile 2***	***Crack profile 3***	***Crack profile 4***
1	3.573	2.847	2.172	2.062	1.859
2	3.365	2.700	2.190	2.068	**1.583**
3	3.009	2.493	2.262	1.931	2.137
4	2.740	2.394	2.252	1.994	1.834
5	2.583	2.370	2.192	2.099	1.835
6	2.518	2.358	2.209	2.088	1.997
7	2.523	2.361	2.248	2.132	2.026
8	2.586	2.402	2.295	2.199	2.098
9	2.704	2.497	2.372	2.278	2.187
10	2.875	2.659	2.502	2.395	2.297
11	3.105	2.889	2.712	2.578	2.465
12	3.406	3.187	3.005	2.857	2.725
13	3.792	3.575	3.389	3.232	3.091
14	4.304	4.079	3.885	3.720	3.570
15	4.970	4.721	4.511	4.329	4.169
16	5.733	5.453	5.218	5.014	4.831
17	6.159	5.849	5.601	5.387	5.195

Table 5.8. Number of cycles to reach each crack profile

Crack profile	***Number of cycles***
1	5,349
2	3,163
3	1,930
4	1,326

5.3.4 Discussion of the Results

As it can be seen from Figures 5.15 and 5.16, for both cases, the crack tends to extend more towards the 100% ceramic side. The crack growth tendency of ceramic with its high value of *n* parameter causes this situation so this is an expected result. But the crack forms are quite different for nearly equal number of cycles. For the modeling of variation along minor axis direction case, near the minor axis towards the right hand side, the tendency of crack growth of ceramic combines with the high stress intensity factor of minor axis so the crack grows towards the ceramic side. For the variation along major axis direction case, the keypoints closer to 100% ceramic side has lower stress intensity factors than the keypoints near the minor axis of ellipse. But their *n* parameter is higher because of being closer to 100% ceramic side. As a result, the crack growth at the keypoints having optimum SIF and *n* values is more. Thus the crack grows by an angle towards the ceramic side.

The total number of cycles are very low compared to the analysis with homogeneous Ti-6Al-4V case. This shows that the change in *n* parameter is dominant against the change in *C* parameter. Addition of ceramic to the structure causes high crack growth rate, thus decreases the number of cycles for constant crack development along minor axis.

Again for both cases, the lowest safety factor values are reached near the keypoints closer to 100% ceramic side. The K_{IC} value of ceramic is about $1/15^{th}$ of metal. Also when the crack extends, the SIF at these keypoints increases and the K_{IC} values decreases. This results in low safety factor values at the keypoints closer to the ceramic side. In the variation along minor axis case, the stress intensity factors of the keypoints near the ceramic side are higher when compared to the variation along major axis case. But the positions of these keypoints are farther to 100% ceramic side. So obtained safety factor values are close to each other for both cases.

CHAPTER 6

CONCLUDING REMARKS

Fatigue crack growth analysis methods for functionally graded materials are developed for two dimensional plane strain and three dimensional cases. The procedures are carried out by writing APDL codes to be run by using ANSYS. The stress intensity factors are determined by displacement correlation technique and Paris – Erdoğan Law is implemented into the study for the crack growth model.

In the first part of the study, the plane strain crack growth model is developed for the test specimens of ASTM standard E399. The stress intensity factors are found for different crack lengths and material variation types. A curve is fitted for each specimen to determine the stress intensity factors for all crack lengths. The fatigue crack growth rate is calculated by writing codes in MATLAB. The material constants are found and the stress intensity factors are read from the curves. It is found that the crack growth rate of specimens with different variation functions can differ very much although the calculated stress intensity factors are very close to each other.

In the second part of the study, elliptical crack growth model in an infinite medium is developed. The procedure is first carried out for homogeneous medium to validate the model with a previous study. The stress intensity factors are found and the crack growth rate is calculated by giving a constant displacement from one of the axis of the crack and the corresponding crack growths for other points along the crack profile. The analysis procedure is extended for functionally graded materials and the material constants effects on the crack development are observed. The results are as expected as the crack growth is observed towards the material which has more tendency of fatigue crack growth.

The analysis procedures described here can be very beneficial in the development of FGM structures. By using these analysis methods, the ceramic and metal materials to be used in a functionally graded material and their variation functions can be determined according to their fatigue crack growth behaviors.

The study described here can be improved for the following situations:

- Fatigue crack growth for arbitrary shaped cracks can be analyzed. Finite element modeling provides the calculation of stress intensity factors for all types of crack geometries.

- The crack growth of cracks in different shaped structures other than infinite volume can be analyzed. In this study, the analysis of consecutive crack forms, are performed with clearing the database and modeling again from the beginning because of the simplicity of infinite medium. Parametric modeling of this medium creates no difficulty. But in some structures that could be a very cumbersome procedure. Instead, part of the model that includes the crack can be modified for the implementation of the new crack profile. Care should be taken in generating the appropriate mesh structure for this case.

- Different cyclic loading types can be analyzed. In engineering applications, generally there exist cases other than mode I loading. Fatigue crack growth rate under mode II mode III loading cases can be determined by developing the code.

- Different boundary conditions simulating the operation of the structures can be modeled.

- Different types of material properties and crack growth models can be applied to the model.

REFERENCES

[1] Functionally Graded Materials, http://www.ntu.edu.sg/mae/research/programmes/adv_materials/FGM.htm, last accessed 02.01.2006

[2] Niido M., Maeda A., Recent Development Status of Functionally Gradient Materials, ISIJ International, Vol. 30, 699-703, 1990

[3] Suemitsu T., Matzuaki Y., Fujioka J., Uchida M.,Sohda Y., KudeY., Uemura S., Kuroda Y., Ueda S., Moro A., Carbon/Carbon Composites for Combustors of Space Planes, Ceamic Transactions, Vol. 34, 315-322

[4] Muller E., Drasar C., Schilz J., Kaysser W.A., Functionally graded materials for sensor and energy applications, Materials Science and Engineering A, Vol. 362, 17–39, 2003

[5] Pompe W., Worch H., Epple M., Friess W., Gelinsky M., Greil P., Hempel U., Scharnweber D., Schulte K., Functionally graded materials for biomedical applications, Materials Science and Engineering A, Vol. 362, 40–60, 2003

[6] Kieback B., Neubrand A., Riedel H., Processing Techniques for Functionally Graded Materials, Materials Science and Engineering A, Vol. 362, 81–105, 2003

[7] Koizomi M., The Concept of FGM, Ceramic Transactions, Vol. 34, 3-10

[8] Plasma Spray Processing of FGMs, http://www.matscieng.sunysb.edu/tsl/fgm/, 2002, Last accessed 26.12.2005

[9] Movchan B.A., Functionally Graded EB PVD Coatings, Surface and Coatings Technology Vol. 149, 252–262, 2002

[10] Movchan B.A., Yakovchuk K. Yu., Graded Thermal Barrier Coatings Deposited by EB-PVD, Surface & Coatings Technology, Vol. 188–189, 85– 92, 2004

[11] Erdogan F., Wu B.H., Analysis of FGM Specimens for Fracture Toughness Testing, Ceramic Transactions, Vol. 34, 39-46, 1993

[12] Ozturk M., Erdogan F., The Axisymmetric Crack Problem in a Nonhomogeneous Medium, ASME Journal of Applied Mechanics, Vol. 60, 406-413, 1993

[13] Fildis H., The Axisymmetric Crack Problem in a Nonhomogeneous Interfacial Region Between Homogeneous Half-Spaces, PhD Thesis, Middle East Technical University, Ankara, 1995

[14] Dag S., Crack Problems in a Functionally Graded Material Under Thermal Stresses, MS Thesis, Middile East Technical University, Ankara, 1997

[15] Yıldırım B., Dag S., Erdogan F., Three Dimensional Fracture Analysis of FGM Coatings under Thermomechanical Loading, Int J Fracture, Vol. 132, 371-397, 2005.

[16] Tilbrook M.T., Rutgers L., Moon R.J., Hoffman M., Fracture and Fatigue Crack Propagation in Graded Composites, Materials Science Forum, Vol. 492-493, 573-580, 2005

[17] Kim J.H., Paulino G.H., Mixed-mode Fracture of Orthotropic Functionally Graded Materials Using Finite Elements and the Modified Crack Closure Method, Engineering Fracture Mechanics, Vol. 69, 1557–1586, 2002

[18] Gu P., Asaro R.J., Cracks in Functionally Graded Materials, Int J Solids Struct, Vol. 34, 1–17, 1997

[19] Ozturk M, Erdogan F., Mode I Crack Problem in an Inhomogeneous Orthotropic Medium. Int J Eng Sci, Vol. 35, 869–883, 1997

[20] Ozturk M, Erdogan F., The Mixed Mode Crack Problem in an Inhomogeneous Orthotropic medium, Int J Fract, Vol. 98, 243–261, 1999

[21] Ural A., Wawrzynek P.A., Ingraffea A.R., Simulating Fatigue Crack Growth in Spiral Bevel Pinion, NASA/CR—2003-212529

[22] Phan A.V., Gray L.J., Kaplan T., Highly Accurate Crack Tip Analysis, Electronic Journal of Boundary Elements, Vol. 1, pp. 51-58, 2002

[23] Kadioglu S., Dag S., Yahsi S., Crack Problem for a Functionally Graded Layer on an Elastic Foundation, Int. J. Fracture, 47 ,533-545

[24] Guo L.C., Wu L.Z., Zeng T., Ma L., Mode I Crack Problem for a Functionally Graded Orthotropic Strip, European Journal of Mechanics A/Solids, Vol. 23, 219-234, 2004

[25] Phan A.V., ANSYS Tutorial 2-D Fracture Mechanics, http://www.southalabama.edu/engineering/mechanical/faculty/phan/ANSYS_LEFM01.pdf, last accessed 30.12.2005

[26] ANSYS Basic Analysis Procedures Guide Release 5.4, Ansys Inc, Canonsburg, PA, ABD-1997., last accessed 30.12.2005

[27] Marrow J., Fatigue Failure,

http://www2.umist.ac.uk/material/research/intmic/schools/schools/fatigue/Default.htm, last accessed 30.12.2005

[28] Key to Metals Task Force & INI International, Key to Steel,

http://www.key-to-steel.com, 2005, Last accessed 30.12.2005

[29] Queen's University, Mech412 - Mechanical Behaviour of Advanced Materials,

http://me.queensu.ca/courses/mech412/Notes/Lecture19.ppt, last accessed 30.12.2005

[30] Paris P. Erdogan F., A Critical Analysis of Crack Propagation Laws, Journal of Basic Engineering – Transactions of the ASME, Vol. 85, 528 – 534, 1963

[31] S. Li, L. Sun, W. Jia, Z. Wang, The Paris Law in Metals and Ceramics, Journal of Materials Science Letters, Vol. 14, 1493-1495, 1995

[32] Engrasp Inc, Fatigue Crack Growth, http://www.engineerstoolbox.com/doc/etb/mod/fm1/paris/paris_help.html, 2003, last accessed 26.12.2005

[33] Matt Gordon, Fracture Toughness and Fracture Design, http://www.sv.vt.edu/classes/MSE2094_NoteBook/97ClassProj/exper/gordon/www/fractough.html, 1997, last accessed 26.12.2005

[34] Automation Creations, MatWeb – The Online Materials Information Source, http://www.matweb.com, last accessed 26.12.2005

[35] Efunda, Inc., Efunda: The Ultimate Online Reference for Engineers, http://www.efunda.com/, last accessed 26.12.2005

[36] Acala J., Aglada M., High-temperature Crack Growth in Y-TZP, Materials Science and Engineering A, Vol. 232, 103-109, 1997

[37] Rudolf M., Jungwirth F., Walter P.O., Threshold Intensity factors as Lower Boundaries for Crack Propagation in Ceramics, Biomedical Engineering Online

[38] ASTM E 399 – 90, Standard Test Method for Plane-Strain Fracture Toughness of Metallic Materials

[39] K-Style Advanced Ceramics, About ZrO2,

http://www.zro2.com/Top-About-ZrO2.htm, last accessed 26.12.2005

[40] Vena P., Gastaldi D., Contro R., Petrini L., Finite Element Analysis of the Fatigue Crack Growth Rate in Transformation Toughening Ceramics, International Journal of Plasticity, Vol. 22, 895-920, 2005

[41] Fort Wayne Metals,

http://fortwaynemetals.com/resources_specsheets/TI%206Al-4V_ELI.pdf, last accessed 26.12.2005

[42] Sanford R.J., Principles of Fracture Mechanics, Prentice Hall, NJ, ABD-2003.

[43] Ritchie R.O., Davidson D.L., Boyce B.L., Campbell J.P., Roder O, High Cycle Fatigue of Ti-6Al-4V, Fatigue and Fracture of Engineering Materials and Structures Vol. 22, 621-631, 1999

[44] Irwin G.R., Crack Extension Force for a Part Through Crack in a Plate, Journal of Applied Mechanics, Vol. 29, 651 – 654, 1962

[45] Martinez-Esnaola J.M., Martin-Meizoso A., Modeling of Fatigue Propagation of Surface Cracks, International J Fracture, Vol. 109,17 – 22, 2001

[46] Joseph P. F., Erdogan F., Surface Crack Problems in Plates, Int J Fracture, Vol. 41, 105 – 131, 1989